electronics

Article

A High-Efficiency High-Power-Density SiC-Based Portable Charger for Electric Vehicles

Stefan Ditze [1,*], Stefan Ehrlich [1], Nikolai Weitz [2], Marco Sauer [1], Frank Aßmus [1], Anne Sacher [1,*], Christopher Joffe [1], Christoph Seßler [1] and Patrick Meißner [1]

[1] Fraunhofer Institute for Integrated Systems and Device Technology IISB, 91058 Erlangen, Germany; stefan.ehrlich@iisb.fraunhofer.de (S.E.); marco.sauer@iisb.fraunhofer.de (M.S.); frank.assmus@iisb.fraunhofer.de (F.A.); christopher.joffe@iisb.fraunhofer.de (C.J.); christoph.sessler@iisb.fraunhofer.de (C.S.); patrick.meissner@iisb.fraunhofer.de (P.M.)

[2] Institute of Power Electronics, Friedrich-Alexander Universität Erlangen-Nürnberg (FAU), 90429 Nuremberg, Germany; nikolai.weitz@fau.de

* Correspondence: stefan.ditze@iisb.fraunhofer.de (S.D.); anne.sacher@iisb.fraunhofer.de (A.S.)

Abstract: This paper proposes a portable 11 kW off-board charger for electric vehicles. In the ac/dc stage, a three-phase power factor correction (PFC) in VIENNA topology is chosen. The loss and volume of the PFC inductance are calculated over a wide range of parameters and optimized with regard to design, winding, and core material. A three-phase LLC resonant converter operating at 1 MHz is chosen for the galvanically isolated dc/dc stage. A parametrizable loss model of the high-frequency transformer and the resonance inductor is developed to minimize volume, weight, and losses. With the help of an automated algorithm using these loss models, the inductive components are optimized in terms of winding specification, magnetic material, and core geometry, verified by finite element analysis and measurements. For the ac/dc stage, 900 V SiC devices are adopted, and 1200 V SiC devices are used in the primary and secondary sides of the dc/dc stage. A variable dc-link voltage is utilized to adjust the charging profile and to operate the LLC resonant converter at the most efficient point near the series resonance frequency. A mechatronically integrated portable air-cooled off-board charger prototype with 11 kW, three-phase 400 V_{AC} input, and 620–850 V_{DC} output is realized and tested. The prototype demonstrates a power density of 2.3 kW/liter (37.7 W/in^3), a peak efficiency of 96%, and 95.8% efficiency over the defined battery voltage range.

Keywords: resonant power conversion; DC–DC power conversion; AC–DC power conversion; battery chargers; mobile power supplies; road vehicle electric propulsion

Citation: Ditze, S.; Ehrlich, S.; Weitz, N.; Sauer, M.; Aßmus, F.; Sacher, A.; Joffe, C.; Seßler, C.; Meißner, P. A High-Efficiency High-Power-Density SiC-Based Portable Charger for Electric Vehicles. *Electronics* **2022**, *11*, 1818. https://doi.org/10.3390/electronics11121818

Academic Editor: Lucia Frosini

Received: 16 May 2022
Accepted: 6 June 2022
Published: 8 June 2022

1. Introduction

The number of available plug-in hybrid electric vehicles (PHEVs) and battery electric vehicles (BEVs) on the market, known commonly as electric vehicles (EVs), has increased significantly in recent years due to the superior properties of the electric powertrain [1], rising fuel costs, and increasing restrictions on the global emission of greenhouse gases [2,3]. All popular EVs are equipped with level-2 conductive on-board chargers (OBCs), which enable the vehicle battery to be recharged at any AC outlet when the car is not in use or at home during the night [4]. As one of the important components in EVs besides battery and powertrain, the performance of OBCs is continuously improved by academia and industry. In the literature, there are various approaches to maximizing system efficiency and minimizing the volume of future OBCs [5–12]. Besides efficient and compact charging solutions, the integration of the auxiliary power module (APM) for the auxiliary battery is becoming more and more important to save costs and construction space [13]. On the part of the automobile manufacturers, the first generation of OBCs is in use, while the second advanced generation is under development or about to be launched in the next generation of EVs [14–21]. Due to the expected high numbers of units, the upcoming OBCs will be further optimized in terms of construction space, reliability, and especially costs.

An overview of OBCs being used in current EVs and optimized chargers that are the subject of literature is given in Figure 1. The system efficiency is plotted versus the power density, as far as these figures are available in the corresponding publications. The type of symbol indicates whether the charger is water-cooled or air-cooled. Presenting the state-of-the-art, the industry-level OBCs are mainly water-cooled for reliability reasons. The chargers operate in the range of 50–150 kHz due to the use of Si technology, resulting in low power densities smaller than 1 kW/liter with efficiencies in the range of 90–94%. New developments focus on efficient SiC semiconductors and optimized passive components, which improve system efficiency to 95% [16,17]. In the literature, the focus is on the application of wide-bandgap (WBG) devices (SiC, GaN) to achieve high switching frequencies above 200 kHz and thus, reduce the size of passive components [5–9]. As shown in Figure 1, the use of WBG devices and the advancement of passive components has continuously increased efficiency and power density limits [7,10,11]. Whiteaker et al. present a very compact 3.3 kW OBC using highly integrated SiC modules for the active front end and the second dc/dc stage [8]. However, efficiency and power density are given without the required EMI filter, which, from experience, reduces the efficiency by 0.5% and raises the system volume by at least 30% (cf. Figure 1) [22]. Using paralleled GaN devices, Lu et al. achieve a very high efficiency of 97% in single-phase charging mode [12]. The first stage operates as an active rectifier switching with line frequency, while the second stage applies the power factor correction and battery charging. Due to the missing dc-link, the battery is charged with double line frequency, which has a negative effect on battery life [23]. For a comparison in Figure 1, the necessary active and passive EMI filters are taken into account by increasing the system volume by 30% and reducing the efficiency by 0.5% [22].

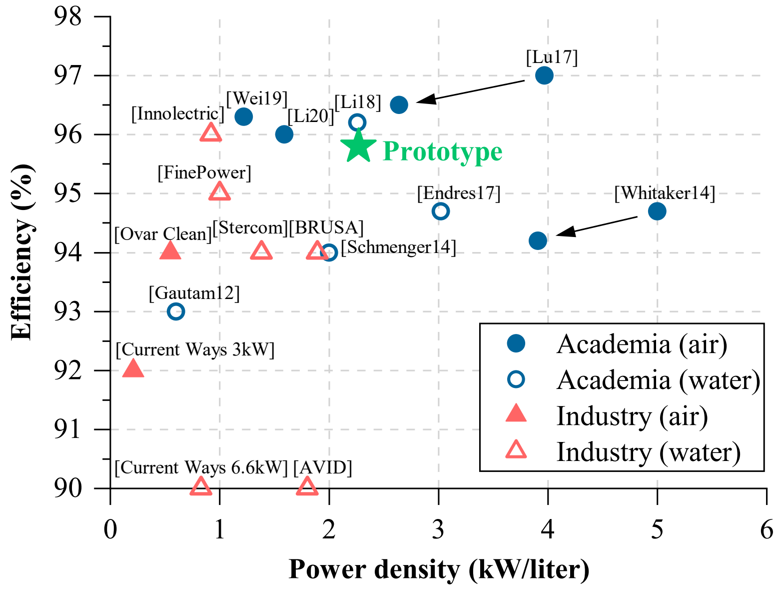

Figure 1. Overview of the state-of-the-art and prototype on-board chargers in terms of efficiency and power density. The shape of the symbol indicates the use of air- or water-cooling.

With the continuing development in the field of EVs, the application of OBCs is also being newly considered. The battery capacity of current and future EVs is forced to increase to alleviate range anxiety. Simultaneously, increasing the battery voltage to 800 V reduces the currents in the HV-power network. Hence, the cross-section of the wiring harness can be reduced, which results in savings in weight and material costs due to less amounts of copper [24]. With the expansion of the dc fast-charging infrastructure and the availability of EVs with an 800 V system, battery charging times can be achieved that are comparable with the refueling of conventional gas vehicles (400 km/250 mi vehicle range in 15 min) [24,25].

Therefore, future vehicles will be equipped as standard with the option of dc fast-charging. The presently installed OBC will thus become less important and, in the long term, will only be offered as an option. This transition from a pre-installed on-board version to a portable charger offers several advantages:

1. The portable charger does not need to be stored in the vehicle if the level-3 dc charging function is mainly used, e.g., at a parking place of retail shops or at the workplace [26]. This releases construction space, which can be used for additional battery capacity and thus extends the range of the EV. Furthermore, the portable charger does not have to comply with automotive standards (lifetime, vibration stress).
2. By using the established dc charging interfaces, a specific charger per vehicle type and manufacturer is not necessary. Portable chargers from different manufacturers would be compatible with each other, resulting in lower costs due to economies of scale, less electronic waste, and simple replacement in case of a defect.
3. The universal approach opens up further possibilities: sharing or temporarily lending a portable charger, mobile charging services, and using the portable charger as a charging station at home.

However, aside from the above-mentioned advantages, the question remains about how the functions of the OBC can be transferred to a portable charging system. In conventional OBCs, the power electronic components are mounted and cooled on a cold plate, which is integrated into the EV's water-cooling system. For the portable design in our study, a cooling solution optimized in weight and size is required. Therefore, the heatsink is mechatronically integrated with the power electronics to achieve the smallest possible volume of the overall system. The remaining empty space in the system can be minimized by proper selection of the size and design of the heatsink, while the cooling performance for the individual components is not compromised and hotspots are avoided.

A commonly published approach to reduce the size of passive components is to increase the switching frequency [6,27]; however, this leads to rising losses in the active devices for hard switching topologies. To minimize the power loss density with increasing switching frequency, the semiconductors must be optimized with regard to technology (Si, SiC, GaN), figure-of-merit (FOM) of the applied device, and packaging. The inductive components must be optimized concerning design, winding structure, and selection of the core material. To maximize the system's performance, the maximum permissible power loss density of the semiconductors and the inductive components must be reached at the nominal operating point of the charger. In general, this maximum power density is linked to a maximum operating temperature of the components, which is determined by the applied cooling solution. Therefore, the optimum of the system design for the portable charger regarding efficiency and power density results at the intersection with the boundary conditions of the heatsink given by cooler performance and size. Although approaches with simplified calculation methods provide quick solutions, the results are subject to considerable uncertainty. Therefore, accurate models of power semiconductors [28] and inductive components [29] are needed to determine the losses over a wide frequency range. Using these models, together with the procedures for creating a virtual prototype, the optimum between system volume and efficiency can be evaluated for different topologies, technologies, and materials.

In this paper, we present a portable off-board charger for future EVs with an 800 V operating voltage. For the selection of the ac/dc converter topology, the relevant PFC topologies are analyzed thoroughly and the PFC inductance is optimized regarding different magnetic materials and switching frequencies. Furthermore, we will demonstrate how a transformer and a resonant inductance for a 1 MHz switching frequency and 800 V input voltage are optimized with respect to the winding structure and the magnetic material using parametrizable loss models and an automated calculation algorithm.

The remainder of this paper is organized as follows: In Section 2, the system specifications of the proposed portable off-board charger are briefly described. The selection and the design of the PFC topology and the optimization of the PFC inductance are presented in Section 3. In Section 4, the design of the 1 MHz LLC resonant converter is introduced and the optimization process of the high-frequency (hf) transformer and the resonant inductance is presented. Section 5 describes the control strategy of the two-stage system, the active rectifier, and the three-phase LLC resonant converter. In Section 6, a mechatronically integrated portable air-cooled off-board charger prototype with 11 kW, three-phase 400 V_{AC} input, and 620–850 V_{DC} output is presented and the performance is verified with measurements. Finally, Section 7 provides discussions and concluding remarks.

2. Portable Off-Board Charger Specification

The universal adoption of the proposed approach requires the utilization of already established dc charging standards. The portable off-board charger itself can be considered a dc charging station and is subject to IEC 61851-23 [30]. To connect the charger on the vehicle side, the combined charging system (CCS) with the Combo 2 plug, according to IEC 62196-3 is used, as it provides the required approval for output voltages up to 1000 V_{DC} [31,32]. Referring to [30], however, when the CCS Combo 2 connector is applied, the use of galvanic isolation between the mains and the vehicle is mandatory. The off-board charger is operated on a three-phase mains supply, common in Europe. A bidirectional operation is not intended at first, as the portable device is an optional accessory for vehicle owners, who charge their vehicles mainly at stationary dc charging stations. Accordingly, it is not assumed that a large number of these chargers will be active at the same time and thus available to the utility companies for vehicle-to-grid (V2G) services. Attached to a wall mount, the portable off-board charger can, however, be used at home as a dc wallbox. For high portability, small dimensions of the charging system, as well as the lowest possible weight, are advantageous in order to simplify handling for the user.

For the 800 V battery of future EVs, an estimation is made on the basis of the available information regarding current lithium-ion cell chemistries as well as reasonable possibilities for the interconnection of the cells in a high-performance battery pack. The voltage range of the vehicle battery is set to a range between 620 V (end-of-discharge voltage) and 850 V (end-of-charge voltage), with a nominal voltage of 800 V. Further specific parameters of the charger are listed in Table 1.

Table 1. Target specification of the portable off-board charger.

Parameter	Value
Input voltage V_{ac}	3~, 400 V_{AC}, 50 Hz
Output voltage V_{Batt}	620–850 V_{DC}
Input power P_{ac}	11 kW
Target weight	5 kg
Target volume	5 L
Charging connector	CCS Combo2
Galv. isolation	mandatory
Thermal management	forced air-cooling

3. AC–DC Converter Stage

3.1. Evaluation of PFC Topology

In the current literature, high-efficiency and high-power-density totem-pole PFC topologies using WBG devices have been demonstrated for applications with single-phase mains [5,27]. Although the authors in [10] have shown that well-known single-phase PFC topologies can also be used in a three-phase network, three-phase PFC topologies offer some advantages. Compared with three individual single-phase PFC rectifier systems, the size of the required dc-link is significantly smaller due to the superposition of the three mains voltages with sixfold mains frequency. Furthermore, fewer components are required than with parallel connected single-phase rectifiers [4,33].

Therefore, from the numerous three-phase active PFC rectifier systems, the following topologies established in industry and academia are selected for closer consideration:

active six-switch boost-type (6S-Boost) PFC rectifier [34], VIENNA rectifier [35], neutral point clamped (NPC) inverter [36], T-type (T^2C) inverter [37], active six-switch buck-type (6S-Buck) PFC rectifier [38], and SWISS rectifier [39]. Considering the maximum rectified voltage of 565 V at the three-phase mains, the 6S-Buck and SWISS rectifier topologies with buck-type characteristics are excluded due to the nominal battery voltage of 800 V and thus with the accompanying necessity to step up the voltage of the PFC in the subsequent dc/dc stage. The NPC and T^2C will not be discussed in the following, as the bidirectional operation is not specified in this approach.

The VIENNA circuit topology, shown in Figure 2a, offers the advantage of a 3-level characteristic, which allows for selecting power transistors with a blocking voltage of half of the peak value of the line-to-line voltage. Furthermore, due to the available three voltage levels, the resulting mains current ripple is reduced and the lower switched voltage leads to a generation of lower conducted EMI noise [33]. The 6S-Boost topology offers a simple structure and requires a minimum number of active components (cf. Figure 2b). However, due to the 2-level characteristic, the switches are stressed by a higher reverse voltage compared to a 3-level topology and the emitted conducted EMI noise is higher [33]. To achieve high power density at low losses for the proposed portable system, in the following, the VIENNA and 6S-Boost PFC rectifier are analyzed and compared in terms of semiconductor losses in detail. First, the switching losses of SiC MOSFETs with different chip sizes, and on-state-resistance R_{DSon}, respectively, are examined by simulation using a double-pulse measuring setup to determine the switch-on energy, $E_{\mathrm{T,on}}$, and the switch-off energy, $E_{\mathrm{T,off}}$. In contrast to the switching loss data in datasheets [36], with this approach, the switching energies at all arising operating points during PFC operation are obtained. Furthermore, in the case of the VIENNA rectifier, the freewheeling diode can be freely selected and thus, the losses in the present configuration are determined, including the dynamic losses of the freewheeling diode. Second, analytical equations are used to calculate the total semiconductor losses over one mains period, considering the dynamic and static loss components. Moreover, the parasitic package inductances and the layout-related commutation inductance are initially neglected, which does not allow for a quantitative but for a qualitative comparison of the two topologies. Thereby, the determined switching energies $E_{\mathrm{T,on}}$, $E_{\mathrm{T,off}}$ and the on-state resistance R_{DSon} of the SiC MOSFETs are stated in Table 2 as well as the forward voltage V_F and the differential resistance r_D of the freewheeling diodes at a 150 °C junction temperature, which are given as input parameters.

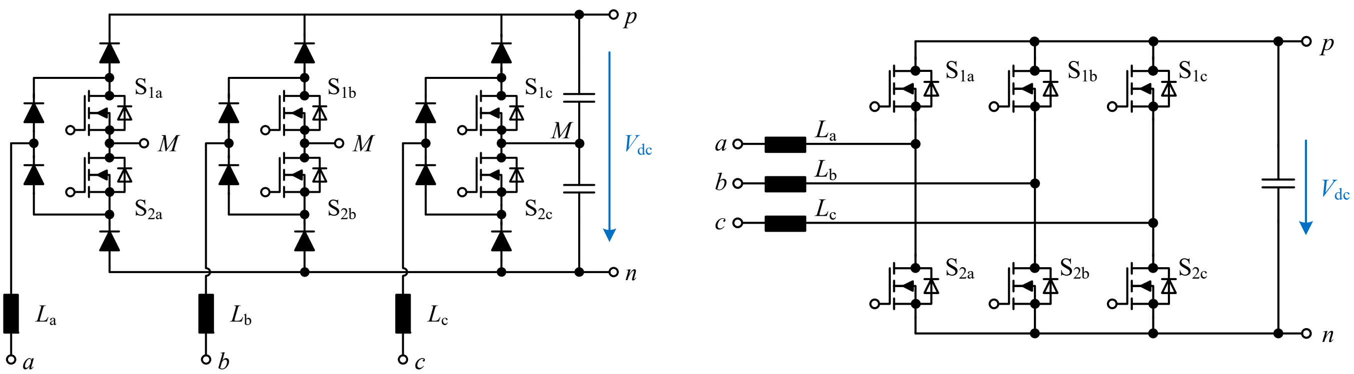

(**a**) (**b**)

Figure 2. Considered topologies for the ac/dc stage: (**a**) VIENNA rectifier; (**b**) active six-switch boost-type (6S-Boost) PFC rectifier.

Table 2. Characteristics of SiC MOSFETs used for comparison.

Topology	Voltage Rating (V)	Current Rating (A)	On-State Resistance R_{DSon} (mΩ)
VIENNA	900	11.5 ... 35	65 ... 280
6S-Boost	1200	30 ... 115	16 ... 75

The conduction losses P_{D} of the mains and the freewheeling diode are modeled by using the piecewise linear approach

$$P_{\mathrm{D}} = V_{\mathrm{F}} I_{\mathrm{D,avg}} + r_{\mathrm{D}} I^2_{\mathrm{D,rms}} \tag{1}$$

with the average current $I_{\mathrm{D,avg}}$ and the root-mean-square (rms) current $I_{\mathrm{D,rms}}$ through the diode. Using the on-state resistance R_{DSon} of the SiC MOSFETs and the rms current $I_{\mathrm{T,rms}}$ through the transistor, the static losses of the MOSFETs can be calculated by:

$$P_{\mathrm{T,stat}} = R_{\mathrm{DSon}} I^2_{\mathrm{T,rms}}. \tag{2}$$

The average and rms value of the device currents are calculated for each switching cycle according to the output current and the present mains voltage. For the VIENNA rectifier, the SiC MOSFET S_{1a} in phase *a* in Figure 2a is controlled with a PWM pulse pattern for the positive line voltage, and S_{2a} for the negative line voltage, respectively. The individual half-bridges in the B6-Boost rectifier can be described as synchronous boost converters, in which the high-side and low-side MOSFETs S_{1a}, S_{2a} in phase *a* in Figure 2b are controlled in each switching period. Therefore, the intrinsic diodes of the MOSFETs only conduct for a short moment during the required dead time between the gate signals of S_{1a} and S_{2a}. Using the data from double-pulse simulation and the calculated current in the PFC inductance, the total switching energy

$$E_{\mathrm{T}} = E_{\mathrm{T,on}} + E_{\mathrm{T,off}} \tag{3}$$

is calculated for all active switches in each switching cycle. The total losses $P_{\mathrm{T,tot}}$ of one MOSFET are derived by integrating the dynamic loss components in (3) over a complete mains cycle. With the static losses given in (2), this results in

$$P_{\mathrm{T,tot}} = P_{\mathrm{T,stat}} + P_{\mathrm{T,dyn}} = P_{\mathrm{T,stat}} + \frac{1}{T_{\mathrm{ac}}} \sum_{m=1}^{\frac{T_{\mathrm{ac}}}{T_{\mathrm{sw,PFC}}}} E_{\mathrm{T},m} \tag{4}$$

with the mains frequency $f_{\mathrm{ac}} = 1/T_{\mathrm{ac}}$ and the switching frequency of the rectifier $f_{\mathrm{sw,PFC}} = 1/T_{\mathrm{sw,PFC}}$. Accordingly, the total losses of all semiconductors can be calculated by

$$P_{\mathrm{semi}} = 6\,(P_{\mathrm{D,ac}} + P_{\mathrm{D,f}} + P_{\mathrm{T,tot}}) \tag{5}$$

with the static losses of the mains side diodes $P_{\mathrm{D,ac}}$ and the freewheeling diodes $P_{\mathrm{D,f}}$.

The comparison of the VIENNA and 6S-Boost topologies is carried out using the parameters listed in Table 3. Due to the 2-level operation principle of the 6S-Boost topology, twice the value is required for the PFC inductance compared to the VIENNA topology. Thereby the topologies become comparable with each other regarding the current ripple and total harmonic distortion of the mains current ($\mathrm{THD_i}$). The distribution of the total semiconductor losses P_{semi} plotted against the switching frequency $f_{\mathrm{sw,PFC}}$ and the drain-source on-state resistance R_{DSon} of the SiC MOSFET, is depicted in Figure 3: in subplot (a) for the VIENNA topology with L_{PFC} = 60 µH, respectively, and in subplot (b) for the 6S-Boost topology using L_{PFC} = 120 µH. The semiconductor losses of the VIENNA rectifier depend on the on-state resistance of the selected SiC MOSFET. In the wide areas of Figure 3a, the semiconductor losses increase linearly with rising on-state resistance at constant switching frequency. Therefore, the static losses $P_{\mathrm{T,stat}}$ in the MOSFET have a dominant influence on total semiconductor loss distribution. Accordingly, the selection of a MOSFET with low R_{DSon} increases the efficiency over a wide range of the considered switching frequency. Furthermore, the losses depend on the static properties of the applied mains side and freewheeling diodes.

Table 3. PFC rectifier parameters used for comparison.

Parameter	Value
Mains voltage V_{ac}	3~, 400 V_{AC}, 50 Hz
DC-link voltage V_{link}	800 V_{DC}
Input power P_{ac}	11 kW
Switching frequency $f_{\mathrm{sw,PFC}}$	50 kHz ... 500 kHz
PFC inductance L_{PFC}	10 µH ... 300 µH

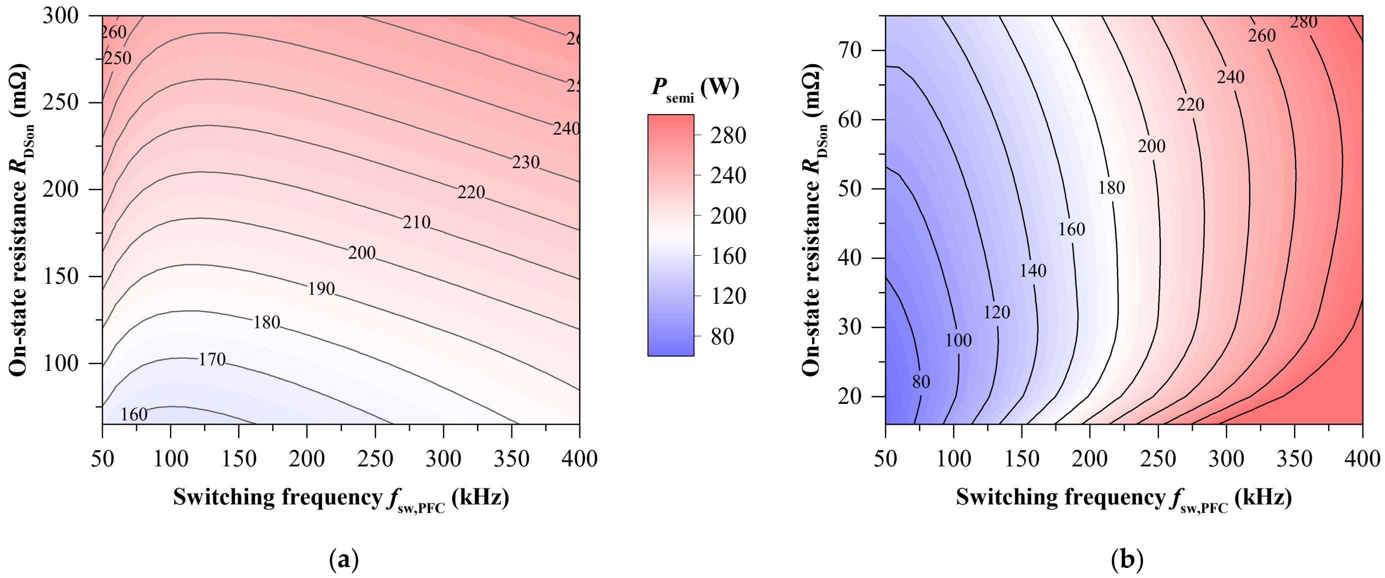

Figure 3. Distribution of the total semiconductor losses P_{semi} versus the switching frequency $f_{\mathrm{sw,PFC}}$ and the drain-source on-resistance R_{DSon} of the SiC MOSFET for (**a**) the VIENNA topology with L_{PFC} = 60 µH (including mains and freewheeling diodes) and (**b**) the 6S-Boost topology with L_{PFC} = 120 µH.

In contrast, at a constant chip size of the applied SiC MOSFETs, the semiconductor losses of the 6S-Boost rectifier rise with increasing switching frequency. According to the contours in Figure 3b, there is an optimum chip size for each switching frequency, which does not necessarily result in the lowest on-state resistance. The authors in [40] found that this optimum is located at the intersection of the dynamic losses P_{dyn} and static losses P_{stat} for the respective chip size, and depends on the transistor current and the switching frequency. With increasing switching frequency, the optimum chip size decreases, i.e., the on-state resistance R_{DSon} rises and the output capacitance decreases.

Although the loss consideration for the B6-Boost topology indicates lower semiconductor losses for $f_{\mathrm{sw,PFC}}$ < 150 kHz, the size and weight of the PFC inductor and heatsink also have to be taken into account in the design of the portable demonstrator. Due to the two-fold lower inductance and the expected lower EMI noise, the VIENNA topology is analyzed in more detail regarding the selection of the MOSFET and the optimization of the inductor. Based on the calculated total semiconductor losses P_{semi} in Figure 3a, a MOSFET with a chip size as large as possible, with low on-state resistance, respectively, should be selected. According to Table 2 and the available types of 900 V SiC MOSFETs from Wolfspeed, a 65 mΩ device (C3M0065090J) is chosen for the following considerations.

To further narrow down the two parameters, switching frequency $f_{\mathrm{sw,PFC}}$ and inductance $\mathrm{L_{PFC}}$, Figure 4 shows the total semiconductor losses for the selected 65 mΩ SiC MOSFET, including the losses in the mains side and freewheeling diodes. The calculated configurations are plotted versus $f_{\mathrm{sw,PFC}}$ and the data points are color-coded with logarithmically distributed values of the PFC inductance. With increasing values of L_{PFC}, the semiconductor losses P_{semi} decrease and reach their minimum at the low switching frequency. Moreover, for values $L_{\mathrm{PFC}} > 150$ µH, equal semiconductor losses can be achieved with different coil configurations, which can be observed by the superimposed arrangement of the mentioned configurations behind the red operating points for $L_{\mathrm{PFC}} = 300$ µH. As a result, the semiconductor losses are mainly determined by the conduction losses due to the high value of L_{PFC} and the dynamic losses at the turn-on instants and turn-off instants, respectively, of the SiC MOSFET, which hardly differ, for the two different inductance values of the PFC coil. Therefore, from the perspective of circuit analysis, the inductance should be selected as high as possible, while at the same time the switching frequency should be low.

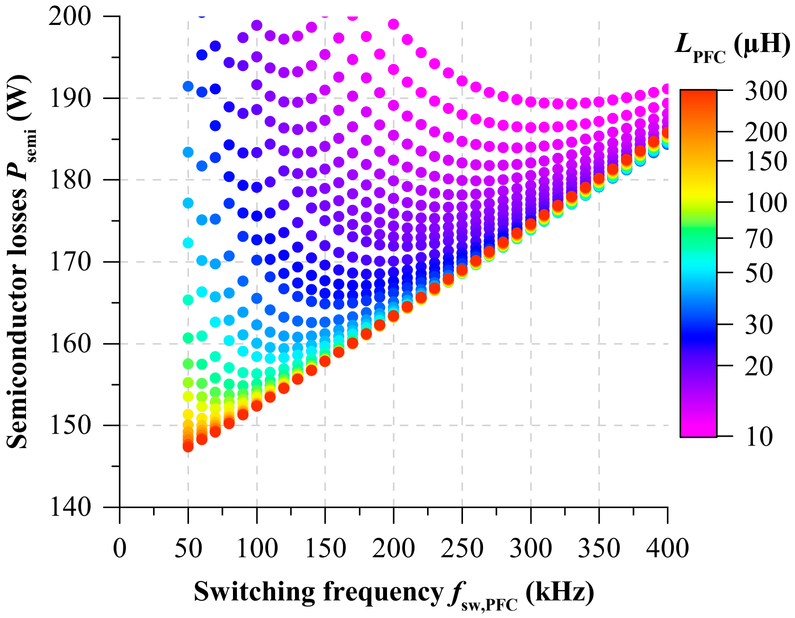

Figure 4. Semiconductor losses of VIENNA topology for SiC MOSFETs with 65 mΩ on-state resistance depending on switching frequency and PFC inductance.

3.2. Inductor Design

Following the suggestion of the preceding topology analysis, to realize the highest possible PFC inductance at a low switching frequency, the process of calculating and optimizing the coil is presented next. Based on analytical calculations, extensive parameter studies are carried out with the aim of determining a Pareto optimum for the power dissipation occurring during operation as a function of the volume of the component and the switching frequency of the PFC. First, the performance of different metal powder-based core materials was compared (Kool Mµ, MPP, High Flux), whereby High Flux turned out to be the most suitable material composition in terms of permeability and losses. For the optimization, a toroidal shape is chosen as the core geometry, which is shown in Figure 5 with the necessary geometrically designations for the following analytical calculation.

To optimize the geometry of the toroidal core without changing the volume of the component, the ratios

$$\begin{cases} \Theta_{\mathrm{C}} = \frac{C_{\mathrm{Tc}}}{A_{\mathrm{Tc}}} \\ \Theta_{\mathrm{B}} = \frac{B_{\mathrm{Tc}}}{A_{\mathrm{Tc}}} \end{cases} \tag{6}$$

are introduced as parameters. As a measure of the required space regarding the system integration, the overall component volume V_{Tc} is defined with the outer diameter A_{Tc} and the height C_{Tc} of the core as follows:

$$V_{\mathrm{Tc}} = \pi \frac{A_{\mathrm{Tc}}^2}{4} C_{\mathrm{Tc}}. \tag{7}$$

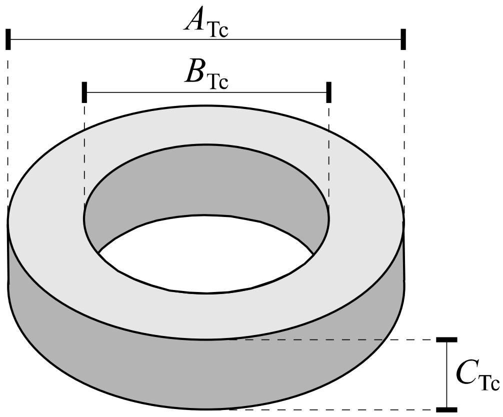

Figure 5. Toroidal core with the geometrical designations for the analytical calculation.

The flowchart describing the optimization strategy for the PFC inductance is shown in Figure 6. Utilizing the data of the operating point of the PFC from Section 3.1, the progression of the coil current $i_{\mathrm{L}}(t)$ is calculated by setting L_{PFC} and $f_{\mathrm{sw,PFC}}$. With the material data and a specified volume V_{Tc}, the core and winding losses in the component are calculated for all combinations of Θ_{B} and Θ_{C}. As a result of this optimization, the optimal coil design is obtained depending on its volume and the selected operating point, which further leads to the representation of a Pareto frontier based on the respective parameter.

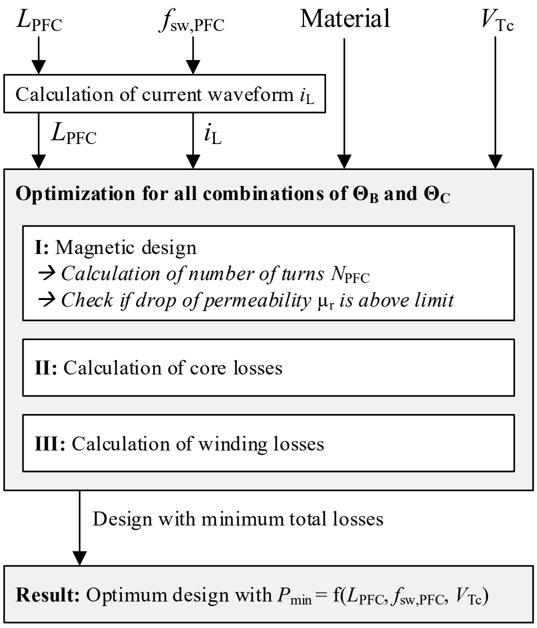

Figure 6. Flowchart describing the optimization strategy for the PFC inductance.

Using the definitions in [41,42], the length of the magnetic path $l_{\mathrm{e,Tc}}$, the magnetic cross-section $A_{\mathrm{e,Tc}}$, and the necessary number of turns N_{PFC} to obtain the selected inductance L_{PFC} can be calculated as:

$$\begin{cases} l_{\mathrm{e,Tc}} = \pi \frac{A_{\mathrm{Tc}} B_{\mathrm{Tc}}}{(A_{\mathrm{Tc}} - B_{\mathrm{Tc}})} \ln\left(\frac{A_{\mathrm{Tc}}}{B_{\mathrm{Tc}}}\right) \\ A_{\mathrm{e,Tc}} = C_{\mathrm{Tc}} \frac{A_{\mathrm{Tc}} B_{\mathrm{Tc}}}{2\,(A_{\mathrm{Tc}} - B_{\mathrm{Tc}})} \left(\ln\left(\frac{A_{\mathrm{Tc}}}{B_{\mathrm{Tc}}}\right)\right)^2 \\ N_{\mathrm{PFC}} = \sqrt{\frac{2\pi \cdot L_{\mathrm{PFC}}}{\mu_0 \mu_{\mathrm{r}} C_{\mathrm{Tc}} \ln\left(\frac{A_{\mathrm{Tc}}}{B_{\mathrm{Tc}}}\right)}}. \end{cases} \tag{8}$$

In comparison to common ferrite materials, metal powder materials show a soft saturation behavior. This effect, however, is not taken into account in the calculation of the time-dependent coil current, but the influence of saturation on the individual loss components is discussed in the following. To exclude too strong saturation effects of the core material during operation, the validity of the calculated results is linked to the condition that, even at the maximum value of the calculated coil current, the permeability of the core material is still at least 60% of its nominal value. Crucial issues arising from temperature-dependent material properties can also be excluded. In a temperature range up to 120 °C, the permeability variations of the considered materials are below 2% of initial permeability. Regarding the core losses, a temperature rise of the core material does not lead to higher losses, since High Flux core losses have a negative temperature gradient [43].

The losses in the core material are determined based on the effective core parameters defined in (8) with the help of a modified Steinmetz equation (MES) [44]. Each switching period $T_{\mathrm{sw,PFC}}$ is considered as a sub-loop in the hysteresis loop of the core material. Since the excitation of the magnetic flux density of the core depends only on the applied voltage time area, the number of turns N_{PFC} and the magnetic cross-section $A_{\mathrm{e,Tc}}$, the non-linearity of μ_{r} can be neglected in calculating the core losses. Using the equations given in [44], for each switching period, the average losses in the core material are calculated and subsequently, the losses caused by the fundamental are superimposed, resulting in the total core losses. Furthermore, the authors in [45] have shown that dc bias has only a minor impact on core losses; therefore, this effect is neglected in the present approach.

For the calculation of the winding losses, first, the turns are evenly arranged along the surface of the toroidal core, according to Figure 7. The diameter of the wire is chosen so that 60% copper and 40% air are present along the dashed line in Figure 7 along the inner circumference. The impact of the skin effect on the winding losses is calculated according to [46]. For the calculation of the proximity losses, it is necessary to determine the magnetic field at each of the N_{PFC} turns around the toroidal core. To simplify the field problem to be solved, the arrangement shown in Figure 7 is assumed to be infinitely extended in the z-direction. This enables the separation of the field problem into two-part problems, as can be seen in Figure 8. For the calculation of the magnetic field of the inner turns, the arrangement shown in Figure 8a is used, while for the outer turns, the arrangement in Figure 8b is applied. In the following considerations the external magnetic fields at the connections between the forward and return conductors are neglected and furthermore, the conductor currents are modeled by line currents I. The magnetic vector potential at the inner turns is expressed by the sum of the vector potentials $A_{1\mathrm{e}}$ and $A_{1\mathrm{s}}$ (cf. Figure 8a). Thereby, $A_{1\mathrm{e}}$ corresponds to the vector potential in the vacuum caused by the line currents; for the calculation of this vector potential, please refer to the literature on field theory. The influence of the core material on the magnetic field is described by $A_{1\mathrm{s}}$, which can be calculated by using the partial derivatives of the magnetic vector potential $A_{1\mathrm{e}}$ at the transition between air and core material:

$$\begin{aligned} &\left.\frac{\partial \vec{A}_{1\mathrm{e}}}{\partial \rho}\right|_{\rho = \frac{B_{\mathrm{Tc}}}{2}} = \\ &= -\vec{e}_{\mathrm{z}} \frac{\mu_0 I}{2\pi} \sum_{\tau=1}^{N_{\mathrm{PFC}}} \frac{\rho_{\mathrm{qi}} \cos(\phi - \phi_{\mathrm{q}\tau}) - B_{\mathrm{Tc}}/2}{\rho_{\mathrm{qi}}^2 + (B_{\mathrm{Tc}}/2)^2 - \rho_{\mathrm{qi}} B_{\mathrm{Tc}} \cos(\phi - \phi_{\mathrm{q}\tau})} \\ &= \vec{e}_{\mathrm{z}} \left(a_{\mathrm{i}0} + \sum_{\upsilon=1}^{\infty} \hat{a}_{\mathrm{i}\upsilon} \cos(\upsilon\phi) \right) \end{aligned} \tag{9}$$

$$
\begin{aligned}
&\left.\frac{\partial \vec{A}_{1e}}{\partial \varphi}\right|_{\rho=\frac{B_{Tc}}{2}} = \\
&= \vec{e}_z \frac{\mu_0 I}{2\pi} \sum_{\tau=1}^{N_{PFC}} \frac{\rho_{qi}(B_{Tc}/2)\ \sin(\varphi-\varphi_{q\tau})}{\rho_{qi}^2+(B_{Tc}/2)^2-\rho_{qi}B_{Tc}\cos(\varphi-\varphi_{q\tau})} \\
&= \vec{e}_z \sum_{\upsilon=1}^{\infty} \hat{b}_{i\upsilon} \sin(\upsilon\varphi)
\end{aligned}
\tag{10}
$$

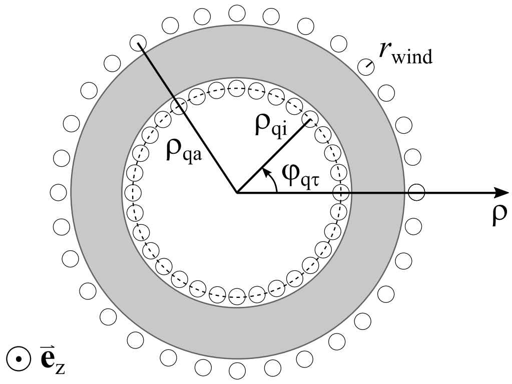

Figure 7. Arrangement of the windings around the toroidal core.

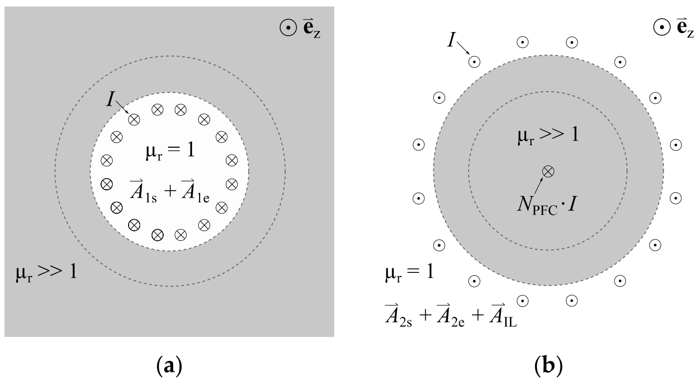

Figure 8. Two parts of the field problem to be solved for the calculation of the magnetic field: for the (**a**) inner windings and (**b**) outer windings.

Applying the Fourier series expansion to (9) and (10), the sought vector potential A_{1s} can be expressed as follows:

$$
\vec{A}_{1s} = \vec{e}_z \sum_{\upsilon=1}^{\infty} \frac{\hat{b}_{i\upsilon} - \mu_r (B_{Tc}/2)\, \hat{a}_{i\upsilon}}{\upsilon\ (\mu_r + 1)} \left(\frac{\rho}{B_{Tc}/2}\right)^{\upsilon} \cos(\upsilon\varphi) \tag{11}
$$

For the field problem to be solved for the outer turns shown in Figure 8b, the influence of the return conductors is described by a single line current with $(N_{PFC} \cdot I)$ lying on the rotational axis; the vector potential caused by this line current is denoted as A_{IL}. For the determination of A_{2s}, again, the partial derivatives

$$
\begin{aligned}
&\left.\frac{\partial \vec{A}_{2e}}{\partial \rho}\right|_{\rho=\frac{A_{Tc}}{2}} = \\
&= \vec{e}_z \frac{\mu_0 I}{2\pi} \sum_{\tau=1}^{N_{PFC}} \frac{\rho_{qa}\cos(\varphi-\varphi_{q\tau})-A_{Tc}/2}{\rho_{qa}^2+(A_{Tc}/2)^2-\rho_{qa}A_{Tc}\cos(\varphi-\varphi_{q\tau})} \\
&= \vec{e}_z \sum_{\upsilon=1}^{\infty} \hat{a}_{a\upsilon} \cos(\upsilon\varphi)
\end{aligned}
\tag{12}
$$

$$\left.\frac{\partial \vec{A}_{2e}}{\partial \varphi}\right|_{\rho=\frac{A_{Tc}}{2}} = \\ = -\vec{e}_z \frac{\mu_0 I}{2\pi} \sum_{\tau=1}^{N_{PFC}} \frac{\rho_{qa}(A_{Tc}/2)\ \sin(\varphi-\varphi_{q\tau})}{\rho_{qa}^2+(A_{Tc}/2)^2-\rho_{qa}A_{Tc}\cos(\varphi-\varphi_{q\tau})} \\ = \vec{e}_z \sum_{\upsilon=1}^{\infty} \hat{b}_{a\upsilon} \sin(\upsilon\varphi) \tag{13}$$

of the magnetic vector potential at the material transition, caused by the remaining line currents, are calculated, and finally the contribution of the vector potential

$$\vec{A}_{2s} = -\vec{e}_z \sum_{\upsilon=1}^{\infty} \frac{(A_{Tc}/2)\ \hat{a}_{a\upsilon} + \mu_r \hat{b}_{a\upsilon}}{\upsilon\ (\mu_r+1)} \left(\frac{\rho}{A_{Tc}/2}\right)^{-\upsilon} \cos(\upsilon\varphi) \tag{14}$$

is determined. Thus, the magnetic vector potential in the area of the turns is determined and the proximity losses in the winding can be calculated by applying the method shown in [46].

To validate the analytical approach for the calculation of the winding losses, these losses are additionally determined by a numerical calculation using the finite element method (FEM). The comparison of both results in Figure 9 shows that the analytically calculated solution predicts higher losses in the winding because the influence of eddy currents occurring in the turns is neglected in the calculation of the magnetic field. Utilizing the described calculation methods, extensive parameter studies are carried out to optimize the geometry, the winding, and the core material of the PFC inductance, with the parameter space considered being summarized in Table 4. As a result, in Figure 10, the total losses versus volume V_{Tc} of the PFC inductor is depicted for different switching frequencies. For each of the plotted data points, all remaining parameters listed in Table 4 are selected to achieve the lowest possible losses and, consequently, Figure 10 illustrates the Pareto optimum of the design at different volumes and switching frequencies. According to the presented results, efficient designs can be realized with increasing volume due to decreasing losses. Since small volumes additionally impose higher demands on thermal management due to increasing power loss density, the minimum volume of the component is limited due to its maximum heat dissipation. Furthermore, the losses also decrease with increasing switching frequency, so higher switching frequencies can contribute to a reduction in the required volume of the PFC inductor. Considering the recommendation made from the perspective of circuit analysis for the selection of inductance and switching frequency in Section 3.1 regarding semiconductor losses and EMC behavior, the switching frequency is set to 140 kHz, as higher frequencies cause only a small reduction in the losses. The volume of the coil is selected at around 30 cm^3, as the expected losses in the range of 10 W lead to a power loss density in the range of 0.3 W/cm^3, which is thermally manageable.

Table 4. Defined parameter space for PFC coil.

Parameter	Value
Core material	High Flux 14 High Flux 26 High Flux 40 High Flux 60
Component volume V_{Tc}	15 cm^3 … 75 cm^3
Geometry ratio Θ_B	0.1 … 0.9
Geometry ratio Θ_C	0.1 … 1
Switching frequency $f_{sw,PFC}$	50 kHz … 200 kHz
PFC coil inductance L_{PFC}	30 µH … 180 µH

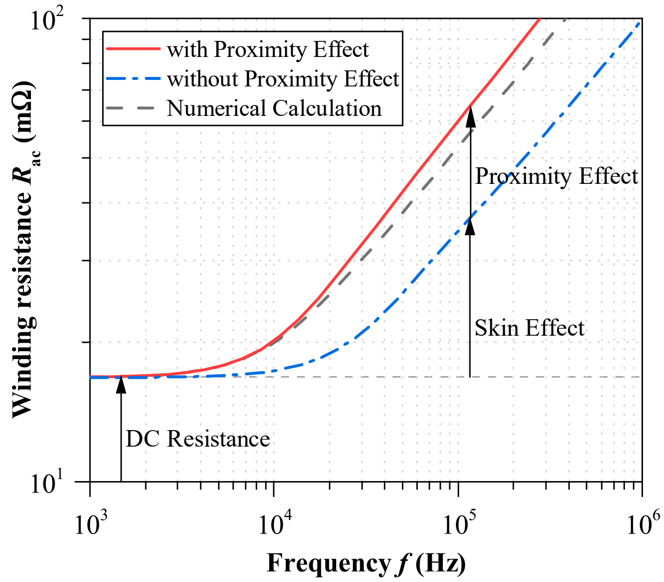

Figure 9. Frequency-dependent resistance $R_{ac}(f)$ of the winding for N_{PFC} = 27 calculated using an analytical approach and numerical method.

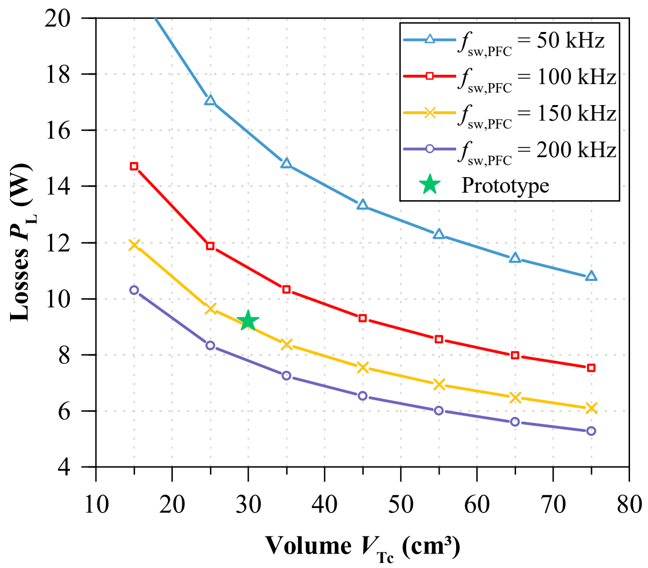

Figure 10. Loss P_L versus volume V_{Tc} of the PFC coil for different selected switching frequencies $f_{sw,PFC}$.

Based on the selection of switching frequency and volume, Figure 11 shows the calculated losses for V_L = 30 cm^3 and $f_{sw,PFC}$ = 140 kHz as a function of the inductance L_{PFC} for different core materials. The core losses increase for the decreasing inductance values, whereas the proportion of winding losses in the total losses increases with the rising inductance values. Following the power dissipation curve for the material "High Flux 60" in Figure 11 to the local minimum, results in an inductance of L_{PFC} = 100 µH for the selected volume and switching frequency. In Table 5, the parameters and results of the chosen optimized PFC coil from Figure 11 and the built prototype are summarized. Due to the availability of a core geometry very similar to the optimal design, the values taken from the Pareto frontier are very well met by the realized prototype, which is shown in Figure 12.

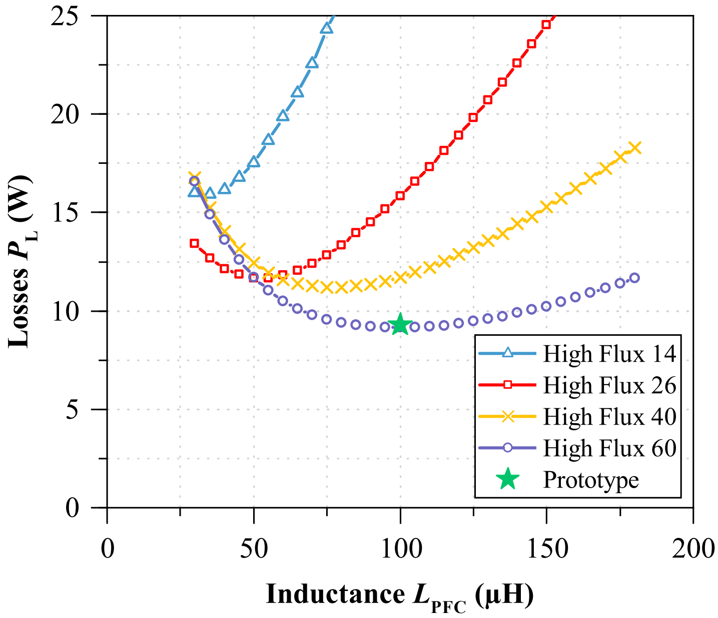

Figure 11. Loss P_L versus inductance L_{PFC} of the PFC coil for different permeabilities at $f_{sw,PFC}$ = 140 kHz and V_{Tc} = 30 cm^3.

Table 5. Optimization results and values of the prototype of the PFC coil.

Parameter	Optimization Result	Prototype
Core material	High Flux 60	High Flux 60
A_{Tc}	45.2 mm	46.7 mm
B_{Tc}	24.9 mm	24.1 mm
C_{Tc}	19.2 mm	18 mm
L_{PFC}	100 µH	100 µH
N_{PFC}	27	27
Winding diameter	1.6 mm	1.5 mm
Sum core loss	4.98 W	4.76 W
Sum winding loss	4.17 W	4.45 W
Total loss P_L	9.15 W	9.21 W

Figure 12. Assembled prototype of the toroidal PFC coil with N_{PFC} = 27.

4. DC-DC Converter Stage

Numerous research projects [47–50] have been focused on the design, modeling, and improvement of LLC resonant converters operating at a switching frequency between 100 kHz and 250 kHz in a wide range of applications. Only a few authors have published results for LLC converters working at frequencies of 1 MHz or higher compared to the voltage and power ranges considered in this publication [51]. The authors in [27] have shown that increasing the switching frequency from 65 kHz to 1 MHz reduces the size of the required passive components by about 50%, which can significantly increase power density. For the LLC converters with switching frequencies greater than 400 kHz, PCB coils and planar integrated transformers are often used [6,51–54]. They are suitable for mass production due to the good reproducibility of the magnetic properties and they achieve high power density due to PCB integration. However, in this paper, the performance of Litz wire-based components at 1 MHz will be investigated due to the following considerations: Compared with Litz wire-based magnetics, PCB integrated magnetics are most sensitive to high-frequency ac winding losses. Operating at 1 MHz, the skin and proximity effect will generate a significant amount of eddy current losses. As a result, the authors in [53] showed that a Litz wire-based transformer has a lower total loss at a similar volume compared to a PCB transformer. Furthermore, Litz wire-based transformers are better suited for integrating and adjusting the necessary leakage inductance [55]. Although the authors in [56,57] have shown that the integration of the resonant inductance is successful for a PCB transformer, however, it is with significantly higher ac winding losses compared to Litz wire. In addition, for a PCB transformer, a thorough design of the primary and secondary windings must be chosen to reduce the resulting intra-winding capacitances as much as possible [58].

The structure of the isolated dc/dc stage using the LLC converter is shown in Figure 13a. It achieves zero voltage switching (ZVS) for the active switches S_{11}–S_{14} on the primary under all load conditions by a proper selection of the resonant parameters. For the rectifier diodes of D_{11}–D_{14} on the secondary, zero current switching (ZCS) can be achieved in a step-up operation. The primary full-bridge applies a square wave voltage with a 50% duty cycle across the resonant tank formed by L_{res}, C_{res}. Due to the low-pass characteristic of the resonant tank, mainly the fundamental component of the applied square wave voltage transfers power to the secondary side and thus charges the battery. The rectifier on the secondary-side conducts according to the polarity of the output voltage v_{sec} of the transformer, e.g., during the positive half-cycle of the transformer output voltage, the secondary resonant current i_{sec} is positive and D_{11}, D_{14} conduct. The output voltage of the LLC converter is controlled by varying the switching frequency $f_{\mathrm{sw,LLC}}$ and is selected to enable converter operation in the inductive range in which the primary resonant current i_{prim} lags behind the applied resonant tank voltage v_{prim}. This ensures that the drain-source voltage v_{DS} across the primary switches has dropped to zero before the resonant current i_{prim} reaches a positive value, providing the condition for ZVS. Detailed operation principles, detailed analysis considering the operating modes, and methods for voltage regulation of the LLC resonant converter can be found in [59–61].

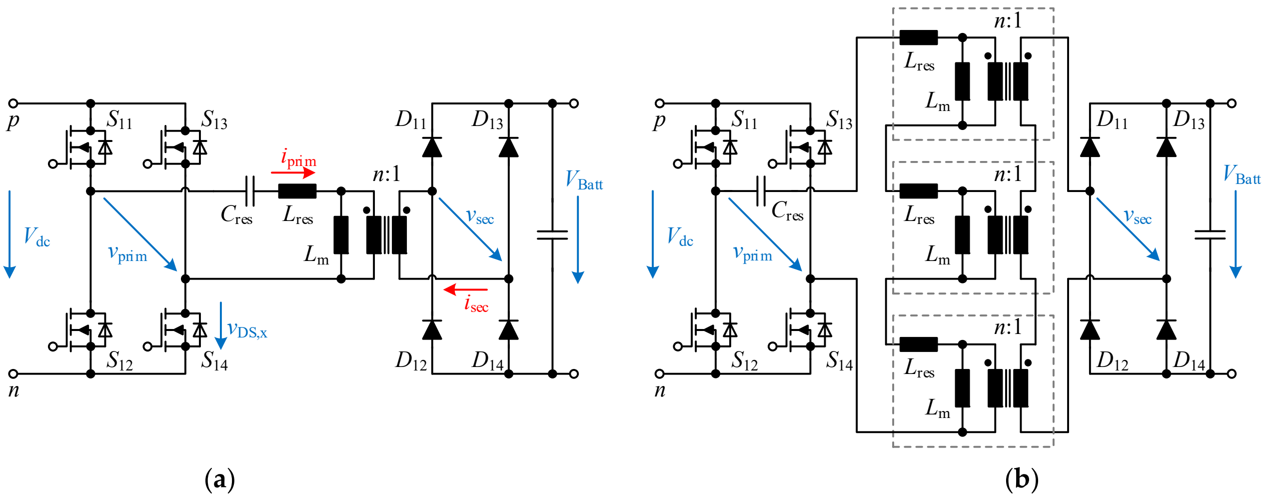

Figure 13. Considered topologies for the dc/dc stage: LLC resonant converter in: (**a**) single-phase implementation and (**b**) single-phase implementation with split transformers.

4.1. Configuration of the LLC Resonant Converter

To handle a large amount of power at a 1 MHz switching frequency, three different design concepts for the LLC converter are considered: single-phase implementation, single-phase implementation with split transformers, and three-phase implementation. With a single-phase implementation, as shown in Figure 13a, the entire power is provided on the primary and secondary sides using a full-bridge inverter and rectifier, which can reduce the required number of semiconductors to a minimum. However, the nonlinear increase in switching energies and the high currents at the turn-off instant of the MOSFETs lead to significantly higher switching losses, which must be thermally dissipated along with the conduction losses that occur. Likewise, the hf transformer is stressed by a high applied voltage and high currents in the primary and secondary windings, which cause significant core and winding losses.

One possibility to reduce the losses in the transformer is to divide the electrical load between three transformers, which are connected in series on the input side and on the output side, as shown in Figure 13b. The three magnetic cores can be selected smaller, in terms of their cross-section and volume, due to the reduced volt-second balance to one third compared with the single-phase configuration. However, on the primary side, each transformer is loaded with the nominal current, which in turn leads to high winding losses. Analysis shows that, due to the high switching frequency, an increase in conductor cross-section does not reduce losses: as the cross-section increases, dc and skin losses decrease, but proximity losses rise to the same extent. A thorough discussion of the loss components of Litz wire-based magnetics can be found in [29]. Moreover, the same high losses occur in the primary and secondary power semiconductors, as already discussed for the single-phase implementation.

In order to increase the efficiency and simultaneously reduce the core and winding losses, a three-phase realization is selected for the dc/dc stage. Although it requires three times the number of semiconductors, they cause significantly lower conduction and switching losses due to the lower load current. Furthermore, the reduction in the load current per phase relieves the hf transformer, which can result in smaller components that can be cooled and integrated more efficiently.

4.2. Design of the LLC Resonant Converter

With a constant 800 V dc-link voltage provided by the VIENNA rectifier, the dc/dc stage has to adapt to the defined battery voltage range (cf. Table 1). This results in a wide switching frequency range to adjust the gain of the resonant converter to the changing battery voltage during charging. However, the LLC converter reaches its most efficient operating point close to the series' resonant frequency:

$$f_{\mathrm{sr}} = \frac{1}{2\pi\sqrt{L_{\mathrm{res}} C_{\mathrm{res}}}}. \tag{15}$$

Thus, the efficiency of the converter decreases for switching frequencies, which deviate significantly from the resonant frequency [47]; at constant dc-link voltage, this applies to wide ranges of the battery voltage. For this reason, a system concept with variable dc-link voltage is implemented [6,47], which offers the possibility of reducing the switching frequency range considerably. Due to the maximum rectified voltage of

$$V_{\mathrm{ac,peak}} = 2\sqrt{2} \cdot 230\ V \approx 650\ V \tag{16}$$

at the three-phase mains, the minimum dc-link voltage is about 750 V considering a 10% tolerance of the mains voltage. Thus, the maximum dc-link voltage variation results in 750–900 V using 650 V rated boost diodes in the VIENNA rectifier and two stacked 500 V dc-link capacitors. The dc-link and battery voltage range are shown in Figure 14, together with the selected gain $M = (n\ V_{\mathrm{Batt}})/V_{\mathrm{dc}} = 1$ of the LLC converter. With a transformer turns ratio of $n = 1.06{:}1$, the converter operates at unity gain within the nominal battery voltage range of 720–820 V. By varying the dc-link voltage accordingly, the switching frequency of the LLC converter stays near f_{sr}, which maximizes efficiency. Below the nominal battery voltage range and near the defined end-of-discharge voltage at 620 V, a phase-shift modulation method can be applied. Above the nominal voltage range, the LLC converter operates with unity gain up to the end-of-charge voltage V_{Batt} = 850 V with V_{dc} = 900 V.

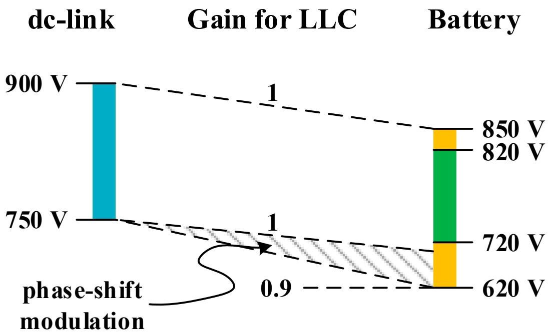

Figure 14. Gain of the LLC converter with n = 1.06 for variable dc-link voltage (750–900 V) covering the nominal battery voltage range.

At the chosen switching frequency of 1 MHz, hard switching of the primary transistors must be prevented to avoid excessive switching losses. Therefore, the magnetizing inductance L_{m} must be selected to ensure that ZVS can be achieved in the given dead time. The output capacitances of the four primary transistors are assumed to be equal and the recharging process is accomplished after

$$t = \frac{2\,C_{\mathrm{oss}} V_{\mathrm{dc}}}{I_{\mathrm{prim}}} \tag{17}$$

where C_{oss} denotes the time-related equivalent output capacitance of each transistor [62]. Due to the operating point at f_{sr}, it is not sufficient to consider only the output capacitances of the transistors at the primary, as the rectifier changes its polarity at the same time the inverter is switching. Accordingly, the junction capacitances of the rectifier diodes are also recharged by the primary resonant current i_{prim}, translated to the secondary. Thus, (17) is extended to

$$t = \frac{2\,\left(C_{\mathrm{oss}} + n^2 C_{\mathrm{j}}\right)\,V_{\mathrm{dc}}}{I_{\mathrm{prim}}} \tag{18}$$

where C_{j} denotes the time-related equivalent junction capacitance of each diode and I_{m} the peak of the primary resonant current. In general, the LLC converter uses the peak of the magnetizing current I_{m}, flowing through L_{m}, to achieve ZVS at the turn-on instant of the transistors, which can be expressed as [62]:

$$I_{\mathrm{m}} = \frac{n\,V_{\mathrm{Batt}}}{4\,L_{\mathrm{m}}\,f_{\mathrm{sw,LLC}}}. \tag{19}$$

At the series resonant frequency f_{sr}, the gain of the resonant tank equals unity, which implies that $n\,V_{\mathrm{Batt}} = V_{\mathrm{dc}}$. Noting that $I_{\mathrm{m}} = I_{\mathrm{prim}}$, the upper limit of L_{m} is obtained by combining (18) and (19) as

$$L_{\mathrm{m}} < \frac{t_{\mathrm{dead}}}{8\,\left(C_{\mathrm{oss}} + C_{\mathrm{j}}\right)\,f_{\mathrm{sw,LLC}}} \tag{20}$$

where t_{dead} denotes the dead time between the high-side and low-side transistor in one phase leg of the primary inverter. Since the capacitances of the power semiconductors do not scale with switching frequency, a dead time of t_{dead} = 100 ns is selected.

Generally, for a specific load condition, $R_\mathrm{L} = V_\mathrm{Batt}/I_\mathrm{Batt}$—the loaded quality factor

$$Q_\mathrm{L} = \frac{\sqrt{\frac{L_\mathrm{res}}{C_\mathrm{res}}}}{n^2 R_\mathrm{L}} \tag{21}$$

known from the fundamental harmonic analysis (FHA), and is used to calculate L_res and C_res [47,63]. However, the FHA does not consider parasitic components (output and junction capacitances) and non-ideal control signals (dead time), which leads to inaccurate results [60]. In order to consider the influence of nonlinear capacitances and dead time on the output power and the ZVS condition, the parameters L_res and L_m are analyzed with a simulative approach. Operating at $f_\mathrm{sw,LLC} = f_\mathrm{sr}$, the LLC converter should achieve the nominal output power $P_\mathrm{LLC,nom}$ at $M = 1$. Further, the phase angle

$$\phi = \angle(v_\mathrm{prim}, i_\mathrm{prim}) \tag{22}$$

should be wide enough to enable ZVS and, at the same time, chosen as small to reduce the reactive power in the resonant tank. In Figure 15, (a) the simulated output power P_LLC, (b) the normalized drain-source voltage $v_\mathrm{DS}/V_\mathrm{dc}$ of the high-side transistor S_{11} at the end of the dead time, and (c) the phase angle ϕ according to (22), are plotted versus L_res and L_m at $M = 1$ and $f_\mathrm{sw,LLC} = 1$ MHz. With increasing values of the magnetizing inductance L_m, the available output power P_LLC starts to decrease, which can be observed in Figure 15a. In comparison, the influence of the resonant inductance L_res on the output power is minor; increasing values of L_res are accompanied by a moderate increase of P_LLC. Thus, it can be determined from Figure 15a that the nominal output power $P_\mathrm{LLC,nom} = 3.6$ kW can be achieved with a magnetizing inductance of 25 µH < L_m < 45 µH, which is initially selected independently of L_res. The considered parameter range is additionally indicated by a red hatched pattern in Figure 15a and is chosen marginally wider, due to the possible deviations of the component parameters in the final design. The achievement of the ZVS condition is illustrated in Figure 15b by the plot of the ratio $v_\mathrm{DS}/V_\mathrm{dc}$ at the end of the dead time. During a soft switching operation, the output capacitances of the transistors are completely recharged to the input voltage V_dc, which in Figure 15b corresponds to a value close to unity and is satisfied in a wide area for the evaluated operating point. The valid parameter range of Figure 15a is thus limited to values 5 µH < L_res < 15 µH, which is indicated by the now reduced red hatched area in Figure 15b. To ensure efficient operation, the phase angle ϕ has to be greater than zero to enable ZVS, but as small as possible to minimize the reactive power circulating in the resonant tank. In order to provide a certain phase margin, a phase angle of $\phi = 25°$ is selected for this design, which in turn significantly limits the valid parameter range, as can be seen in Figure 15c.

According to the previously discussed design considerations, a resonant inductance of $L_\mathrm{res} = 15$ µH and a magnetizing inductance of $L_\mathrm{m} = 39$ µH are selected from Figure 15c. In order to operate the LLC converter slightly in step-up mode and thus enable ZCS at the rectifier, the series resonance is selected 20 kHz higher than the switching frequency. Using (15) and $f_\mathrm{sr} = 1.02$ MHz, the value of the resonant capacitor is calculated at $C_\mathrm{res} = 1.62$ nF. The design parameters for one phase of the LLC converter are summarized in Table 6.

Table 6. Specification of the LLC resonant converter.

Parameter	Value
Input voltage V_dc	750–900 V_DC
Output voltage V_Batt	620–850 V_DC
Number of phases	3
Nominal output power per phase $P_\mathrm{LLC,nom}$	3.6 kW
Switching frequency $f_\mathrm{sw,LLC}$	1 MHz
Resonant frequency f_sr	1.02 MHz
Primary MOSFET	C3M0065100J

Table 6. *Cont.*

Parameter	Value
Equivalent output capacitance MOSFET C_{oss}	70 pF
Secondary diode	IDM10G120G5
Equivalent output capacitance diode C_j	60 pF
Dead time t_{dead}	100 ns
Transformer turns ratio n	1.06:1
Resonant capacitance C_{res}	1.62 nF
Resonant inductance L_{res}	15 µH
Magnetizing inductance L_m	39 µH
Target volume of transformer and inductance	0.1 L

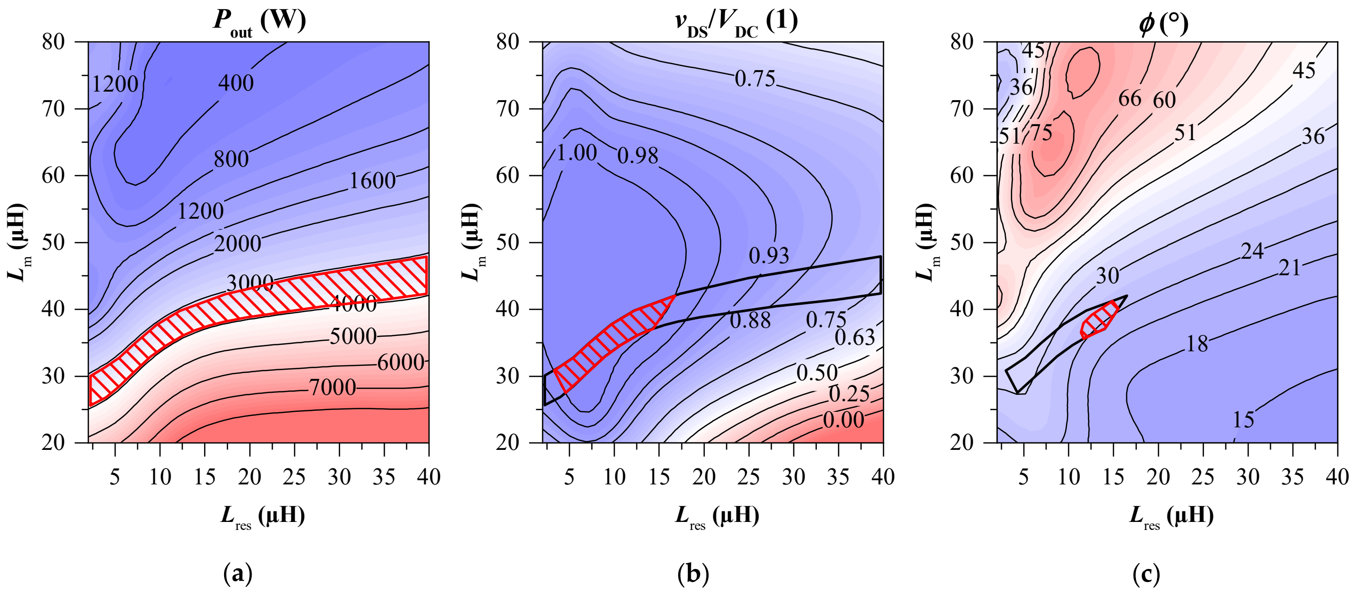

Figure 15. Parameter sweep of the magnetizing inductance L_m and resonant inductance L_{res} at $f_{sw,LLC}$ = 1 MHz, M = 1 using simulation. The red hatched pattern indicates the valid parameter range for (**a**) the simulated output power P_{out}, (**b**) the ZVS condition of the primary inverter, and (**c**) the phase angle ϕ.

4.3. HF Transformer and Resonance Inductor Design

To achieve the required power density, efficiency, and high switching frequency, the optimized magnetic components are indispensable. First, the modeling of the core geometry and the calculation of the magnetic fields in the core and winding window for the transformer and resonance inductor are briefly explained. This is followed by a short description of the optimization process, and finally, a discussion of the results.

Considering commonly used geometries, the E-cores and their variations (E, ER, and PQ) are selected for the following calculations. The geometrical dimensions of the E-core are depicted in Figure 16, where A_{Ec} and $2{\cdot}B_{Ec}$ are the length and height of the core, and M_{Ec} and $2{\cdot}D_{Ec}$ are the length and height of the winding window. With the depth of the core C_{Ec}, the total volume V_{Ec} of this arrangement is defined as follows:

$$V_{Ec} = 2A_{\,Ec}B_{\,Ec}C_{\,Ec}. \tag{23}$$

In order to achieve a homogeneous magnetic flux density distribution and thus reduce the core losses, the magnetic cross-sections are selected as the same in all subsections of the magnetic core. To reduce the number of geometric dimensions, the ratios

$$\begin{cases} \chi_{BA} = \frac{B_{Ec}}{A_{Ec}} \\ \chi_{CA} = \frac{C_{Ec}}{A_{Ec}} \\ \chi_{w} = \frac{2M_{Ec}D_{Ec}}{A_{Ec}B_{Ec}} \end{cases} \tag{24}$$

of the outer dimensions of the E-core and the winding window are defined. With a copper filling factor ρ_w, the maximum diameter of a round Litz wire can be calculated as

$$d_{li} = 2\sqrt{\frac{\rho_w A_w}{N\pi}} \tag{25}$$

where $A_w = 2M_{Ec}D_{Ec}$ defines the size of the winding window, and N is the total number of turns. Assuming a Cartesian coordinate system (x, y) within the winding window of width w_x and height w_y (cf. Figure 16), the N turns are placed in a manner, that each of them takes the largest possible distance from the air gap with length l_g and, thus, reducing the proximity losses due to the stray fields to a minimum.

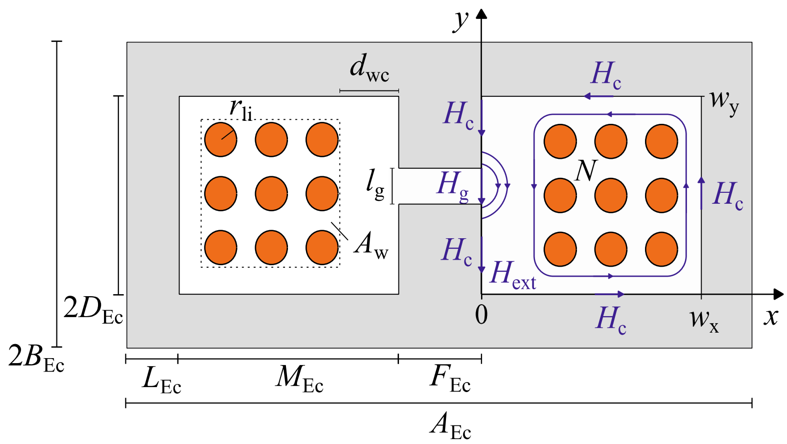

Figure 16. Cross-section of E-core winding arrangement with air gap. The schematic representation is assumed to be infinitely in z-direction.

Assuming a fixed inductance value L, the core geometry parameters V_{Ec}, χ_{BA}, χ_{CA}, χ_w, the filling factor ρ_w, and the number of turns N remain as tuning parameters and, thus, remain as degrees of freedom for the efficiency-optimal design of the hf transformer and the resonance inductor. The calculation of the core geometry parameters as a function of the tuning parameters can be summarized as follows:

$$\begin{cases} A_{Ec} = \sqrt[3]{\frac{V_{Ec}}{2\chi_{BA}\chi_{CA}}}, B_{Ec} = \chi_{BA}A_{Ec} \\ C_{Ec} = \chi_{CA}A_{Ec} \\ D_{Ec} = \frac{1}{8}\left[4B_{Ec} - A_{Ec} + \sqrt{(A_{Ec} - 4B_{Ec})^2 + 16A_{Ec}B_{Ec}\chi_w}\right] \\ F_{Ec} = \frac{1}{2}(A_{Ec} - 2M_{Ec}) \\ M_{Ec} = \frac{A_{Ec}B_{Ec}\chi_w}{2D_{Ec}} \end{cases} \tag{26}$$

$$\begin{cases} l_e = \frac{C_1^2}{C_2} \\ A_e = \frac{C_1}{C_2} \\ V_e = l_e A_e \\ L = \frac{\mu_0 N^2}{\frac{1}{\mu_r}\left(C_1 - \frac{l_g}{A_c}\right) + \frac{l_g}{A_g}} \\ A_c = F_{Ec}C_{Ec} \\ A_g = A_c + l_g\frac{C_{Ec}+F_{Ec}}{2}\ln\left(\frac{4D_{Ec}}{l_g}\right) \end{cases} \tag{27}$$

Considering the large number of tuning parameters, the magnetic parameters for the optimization process are calculated by analytical equations, which are summarized in (27). To determine the magnetic parameters in (27), the magnetic path length l_e, magnetic cross-section A_e, effective core volume V_e, and the core factors C_1 and C_2 are used, which are derived from the core geometry parameters according to [41,42]. Furthermore, the self-inductance L of any winding arrangement with N turns within the E-core can be calculated with the analytical formulas according to [41,42]. Thereby, A_c represents the geometric cross-section of a core section and A_g represents the effective expansion of the magnetic cross-section in the air gap. Using (27) for the determination of A_g leads to good results for small air gaps [41,64]. To realize a desired inductance value L, the length of the air gap l_g is adjusted for a given number of turns N.

The losses in the core material are determined with the help of the corresponding Steinmetz parameters and modified Steinmetz equation (MSE) [44,65]. The magnetic flux density in the magnetic core is determined by the magnetizing current, the magnetic cross-section A_e, and the number of turns N. Skin losses in the Litz wire are calculated with the analytical Bessel formulas according to [41]. Thereby, the connections between the forward and return conductors, which are not shown in the two-dimensional view in Figure 16, are also taken into account. In order to consider the proximity losses in the winding, it is necessary to determine the magnetic field at each of the N turns in the winding window. To reduce the calculation effort on a personal computer, the field problem is simplified to a two-dimensional problem. According to [41,46], the entire coil arrangement is assumed to be infinitely extended in the z-direction, with the magnetic field having only components in the x- and y-direction (cf. Figure 16). Furthermore, to limit the number of tuning parameters, only one air gap centrally located in the center leg of the E-core is considered. The field problem, however, can be extended to the distributed air gaps and the air gaps in the outer legs of the E-core using the same approach. In the following consideration, the external magnetic fields at the connections between the forward and return conductors are neglected and, furthermore, the conductor currents are modeled by line currents with i_n = 1 A. The total external magnetic field is obtained by calculating the field distribution of each individual turn and the subsequent superimposition of all fields.

To calculate the magnetic field distribution in the winding window, the boundary value problem for a single turn must be solved and the solutions are superimposed afterwards. The most important steps for the calculation of the solution are shown in the following; all these steps are carried out according to the procedure described in [41]. Depending on the magnetic parameters defined in (27), the analytic solution of the magnetic field in the air gap

$$H_g = \frac{i_n}{A_g}\left[\frac{1}{\mu_r}\left(C_1 - \frac{l_g}{A_c}\right) + \frac{l_g}{A_g}\right]^{-1} \tag{28}$$

and the magnetic field in the core

$$H_c = \frac{i_n}{\mu_r A_c}\left[\frac{1}{\mu_r}\left(C_1 - \frac{l_g}{A_c}\right) + \frac{l_g}{A_g}\right]^{-1} \tag{29}$$

are derived [41,46]. To calculate the magnetic field around the turns, the first boundary conditions for the fields in (28) and (29) are formulated: while for the boundaries at $x = w_x$, $y = 0$, and $y = w_y$, the tangential component of the magnetic field is assumed to be constant:

$$\begin{cases} H_x(x)\big|_{y=0} = H_y(y)\big|_{x=w_x} = H_c \\ H_x(x)\big|_{y=w_y} = -H_c \end{cases} \tag{30}$$

Differentiation for the tangential component is made at the boundary $x = 0$ as follows:

$$H_{\mathrm{y}}(y)|_{x=0} = \begin{cases} -H_{\mathrm{c}}, & 0 \leq y < D_{\mathrm{Ec}} - l_{\mathrm{g}}/2 \\ -H_{\mathrm{g}}, & D_{\mathrm{Ec}} - l_{\mathrm{g}}/2 \leq y < D_{\mathrm{Ec}} + l_{\mathrm{g}}/2 \\ -H_{\mathrm{c}}, & D_{\mathrm{Ec}} + l_{\mathrm{g}}/2 \leq y \leq 2D_{\mathrm{Ec}} \end{cases} \tag{31}$$

Second, the exciting magnetic field is subtracted from the original fields at the boundaries, so that only the Laplace equation within the winding window has to be solved. The solution to the boundary field problem results in the magnetic field components in the x- and y-direction at the conductor positions (x, y) in the winding window with

$$\begin{aligned} H_{\mathrm{x,n}}(x,y) = {} & B_0 + C_0 x - 2D_0 y - \frac{i_{\mathrm{n}}}{2\pi}\frac{y-y_{\mathrm{n}}}{(x-x_{\mathrm{n}})^2+(y-y_{\mathrm{n}})^2} \\ & -\sum_{\iota}\left(\left(E_\iota \cosh(\iota(x-w_{\mathrm{x}})) + F_\iota \cosh(\iota x)\right)\sin(\iota y)\iota\right) \\ & +\sum_{\iota}\left(\left(G_\iota \sinh\left(\iota\left(y-w_{\mathrm{y}}\right)\right) + H_\iota \sinh(\iota y)\right)\cos(\iota x)\iota\right) \end{aligned} \tag{32}$$

and

$$\begin{aligned} H_{\mathrm{y,n}}(x,y) = {} & -A_0 - C_0 y - 2D_0 x + \frac{i_{\mathrm{n}}}{2\pi}\frac{x-x_{\mathrm{n}}}{(x-x_{\mathrm{n}})^2+(y-y_{\mathrm{n}})^2} \\ & -\sum_{\iota}\left(\left(E_\iota \sinh(\iota(x-w_{\mathrm{x}})) - F_\iota \sinh(\iota x)\right)\cos(\iota y)\iota\right) \\ & +\sum_{\iota}\left(\left(G_\iota \cosh\left(\iota\left(y-w_{\mathrm{y}}\right)\right) + H_\iota \cosh(\iota y)\right)\sin(\iota x)\iota\right) \end{aligned} \tag{33}$$

where $(x_{\mathrm{n}}, y_{\mathrm{n}})$ describes the position of the n-th exciting conductor, ι is the summation index, and $A_0 - D_0$ as well as $A_\iota - D_\iota$ are constants determined by the boundary field problem. The practical implementation showed that sufficient convergence is achieved with the termination of the sum at $\iota = 400$. Assuming the external magnetic field to be homogeneous over the conductor cross-section, proximity losses in the round turns are calculated according to [41]. The described procedure does not take into account the influence of current displacement in round conductors on the characteristics of the external field at the individual turns. However, this influence has only a minor effect on the accuracy of the loss calculation when using high-frequency Litz wires [29].

The flowchart describing the optimization strategy for inductive components is shown in Figure 17. In the first step, the specification and the boundary conditions are defined. It is assumed, however, that the currents of the individual turns can be described analytically or are otherwise known for the operating point under investigation. Since each turn can be excited individually, the procedure is not limited to the inductors. After selecting the tuning parameters, the parameter space is sampled evenly, whereby the configuration with the lowest losses is selected for each volume V_{Ec}. These points serve as input parameters for an optimization based on the MATLAB function `fminsearch()` and result in a loss versus volume plot.

The specification of the resonant tank parameters and the switching frequency $f_{\mathrm{sw,LLC}}$ are listed in Table 6. Due to the selected high switching frequency of 1 MHz, the high-performance ferrite material Fi337 from SUMIDA Components & Modules GmbH, and a Litz wire with a strand diameter of d_{s} = 0.05 mm from Elektrisola GmbH, are selected. The number of turns N_{p}, N_{s} is determined from the diameter d_{li} according to (25), and a typical copper fill factor of a Litz wire is assumed [41,66]. In general, the integration of the resonance inductance as leakage inductance directly into the transformer offers advantages in terms of a reduction in components, costs, and construction space. However, the utilization of the leakage flux significantly reduces the efficiency of the component due to high proximity losses in the windings at 1 MHz. Therefore, the resonant inductance is not integrated into the transformer but designed as an external component. As a result, a coupling of almost unity results in the best possible compensation of the primary and secondary currents in the hf transformer and the magnetizing inductance L_{m}, the resonance inductance L_{res}, and the number of turns ratio n can be tuned more precisely, leading to efficient and compact components.

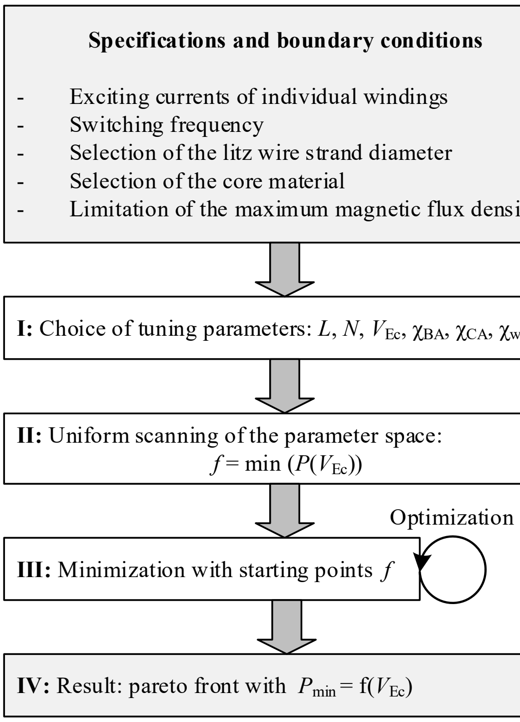

Figure 17. Flowchart for optimal design of inductive components.

As the degrees of freedom and parameters of the optimization process remain the normalized parameters of the core geometry, the volume of the transformer $V_{Ec,tr}$, the resonance inductance $V_{Ec,res}$ as well as the number of turns of the transformer N_p, N_s, and the resonance inductance N_{res}, are listed in Table 7.

Table 7. Tuning parameters for a loss-optimized design of the hf transformer and resonance inductor.

Parameter	Range
Transformer: number of turns (primary) N_p	5, 10, 16, 20
Transformer: number of turns (secondary) N_s	5, 10, 16, 20
Resonance inductor: number of turns N_{res}	1 ... 10
Core geometry ratio χ_{BA}	0.2 ... 2
Core geometry ratio χ_{CA}	0.2 ... 2
Winding window ratio χ_{w}	0.1 ... 0.9
Filling factor of Litz wire in the winding window ρ_w	0.05 ... 0.7
Volumes $V_{Ec,tr}$, $V_{Ec,res}$	0.01 L ... 1 L

As a result, in Figure 18, the total loss versus volume of (a) the transformer and (b) the resonance inductor is depicted for the different number of turns and optimized geometric parameters. According to Figure 18a, a higher number of turns results in lower losses for transformers with small volumes $V_{Ec,tr}$. This is primarily due to the core losses, which increase for ferrites with exponents greater than two to the magnetic flux density in the core and thus, a certain number of turns is necessary to limit the magnetic flux density. Above a certain number of turns, the proximity losses in the windings increase more strongly, whereas, for comparatively large volumes, the conduction losses in the windings dominate, which is why low numbers of turns lead to low losses. As the volume $V_{Ec,tr}$ increases, the losses in the represented range decrease; up to a volume of 0.05 L, they decrease to about half of their initial value and decrease only slightly for larger volumes. The same behavior of the losses as a function of the volume is also observed for the resonance inductance seen in Figure 18b, where a variation of the number of turns in the range 1 to 10 is considered. By limiting the total volume for the inductive components to less than 0.1 L, configurations for the transformer at $V_{\mathrm{Ec,tr}} = 0.054$ L with $N_{\mathrm{p}} = 16$ and for the resonance inductance at $V_{\mathrm{Ec,res}} = 0.028$ L are selected. From the Pareto frontier solutions in Figure 18, the optimal values of the geometric and magnetic parameters are obtained for each point. For the selected transformer and resonance inductance designs, the effective magnetic cross-section A_{e} versus volume $V_{\mathrm{Ec,x}}$ (transformer: $V_{\mathrm{Ec,tr}}$, inductor: $V_{\mathrm{Ec,res}}$) is shown in Figure 19a, respectively, for the air gap length l_{g} in Figure 19b.

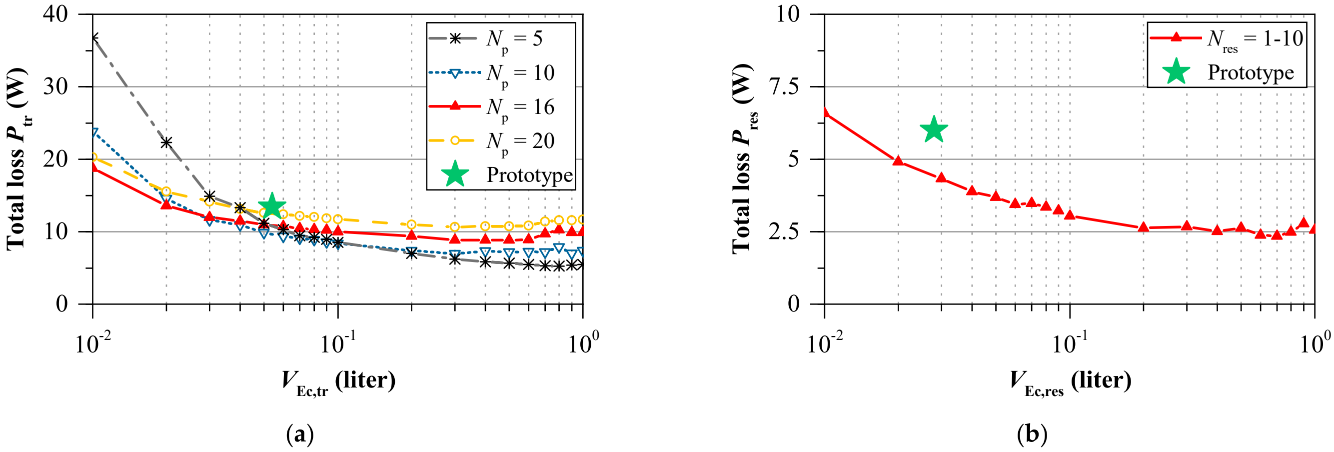

Figure 18. Loss P versus volume $V_{\mathrm{Ec,x}}$ Pareto frontier for (**a**) the transformer and (**b**) the resonance inductance.

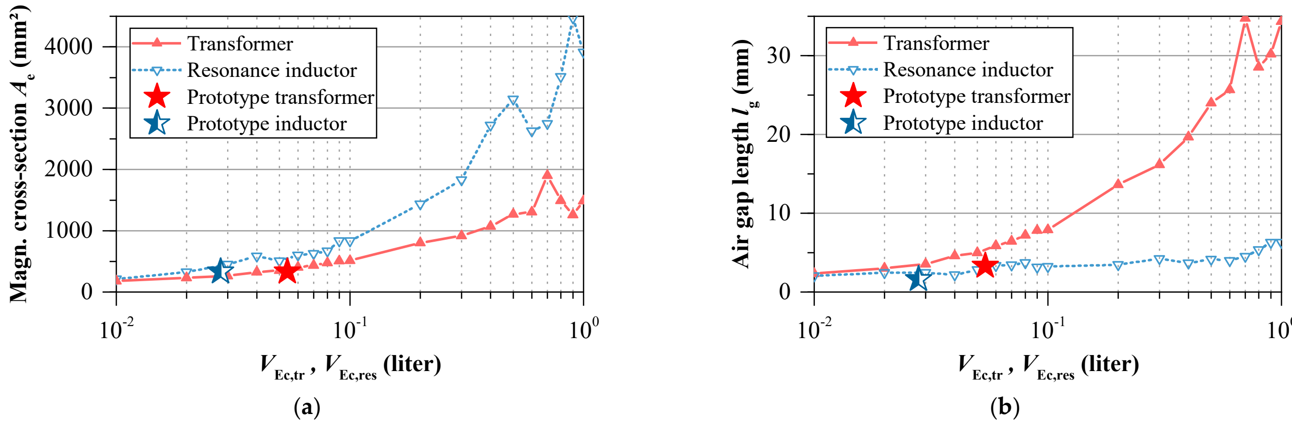

Figure 19. Efficiency-optimal design parameters of the inductive components as a function of volume $V_{\mathrm{Ec,x}}$ and under consideration of the boundary conditions in Table 7. (**a**) Effective magnetic cross-section A_{e} and (**b**) length of the air gap l_{g}. For the transformer, $N_{\mathrm{p}} = 16$ is selected.

The preceding sensitivity analysis, using analytical equations, helps to limit the parameter space defined in Table 7 in order to exclude the unfavorable parameter combinations with respect to the losses. Based on the design parameters, which, according to Figure 18 lead to the prototypes with losses near the Pareto frontier, PQ50 cores are selected to realize the inductive components. While the required magnetic cross-section A_{e} corresponds well to the selected geometry, the height of the core halves is adjusted to the ideal magnetic path length l_{e} to build the transformer. The leakage flux in the winding window and thus the proximity losses in the windings are reduced by a triple distributed air gap. The height of the ferrite plates used to realize the air gaps follows the results in [67].

In the selected design, the resonance inductor is not implemented as a single component but is attached directly to the transformer. A part of the lower half of the magnetic core of the transformer serves as a magnetic return path, which means that volume can be saved compared to the calculated ideal design parameters. In Figure 20a, the prototype design of the inductive component is shown, including the geometric dimensions. To verify the aforementioned analyses and the results of the optimization strategy, a finite element method (FEM) based 3D model for the transformer and the resonance inductance is developed using ANSYS Maxwell. Figure 20b illustrates the FEM simulation results of the maximum magnetic flux density at the nominal operating point ($f_{\mathrm{sw,LLC}}$ = 1 MHz, I_{prim} = 7.6 A, I_{sec} = 6.5 A), which is used to calculate the core losses for the selected Fi337 material. On average, the core is excited with a maximum value of 40 mT, which corresponds to an average power loss density of 150 kW/m^3 at room temperature compared to the loss measurements on the toroidal core samples of the same material [68]. In summary, the calculated results and the results determined by the FEM simulation for the winding and core losses are listed in Table 8. The results of both methods are consistent and follow similar trends.

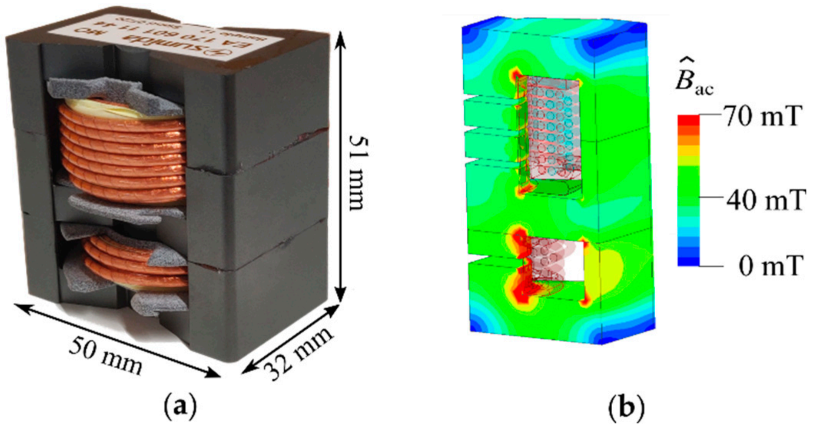

Figure 20. Image of (**a**) the built transformer and resonance inductance and (**b**) the simulated magnetic flux density.

Table 8. Simulated and measured losses of the hf transformer and resonance inductor.

Loss (W)	3D Simulation	Measurement
Transformer winding loss	9.3	-
Inductor winding loss	2.4	-
Sum winding loss	11.7	10.5
Transformer core loss	6.4	-
Inductance core loss	4.5	-
Sum core loss	10.9	-
Total loss	22.6	23.8

5. Control Strategy

5.1. Two-Stage System Control

As previously described, the ac/dc stage performs the PFC function and controls the battery charging current. The LLC converter can thus be operated at a constant switching frequency as a dc transformer, thereby achieving high efficiency over a wide battery voltage range [6].

The VIENNA rectifier is controlled by three control loops, which are shown in Figure 21. To simplify matters, only one mains' phase of the rectifier with the corresponding control is shown in Figure 21; the other two phases are each provided with their separate current control loop.

1. The red control loop realizes the peak current mode control, the current limitation, and the PFC function. The current through the MOSFETs is sensed by a shunt, which is inserted between the MOSFETs and the "*M*" potential. A detailed description of the peak current mode control can be found in [69].

2. The blue control loop is the outer voltage control loop for the dc-link, which also balances the voltage across the series-connected dc-link capacitors to ensure that they are uniformly loaded with $V_{dc}/2$ during operation. Only one voltage control loop is implemented, and the control value is passed to all three PFC current controllers.
3. A charge controller realizes the different charging modes "constant current" (CC), "constant power" (CP), and "constant voltage" (CV), which is shown in orange. A PI controller compares the measured output current multiplied by the battery voltage with the target output power. In addition, the current system temperatures are taken into account for the implementation of a derating function, which reduces the nominal value of the charging power depending on the thermal conditions. The control value of the charge controller is passed to the input of the blue voltage control loop and thus for the dc-link voltage, which is varied according to the current battery voltage and state of charge, respectively.

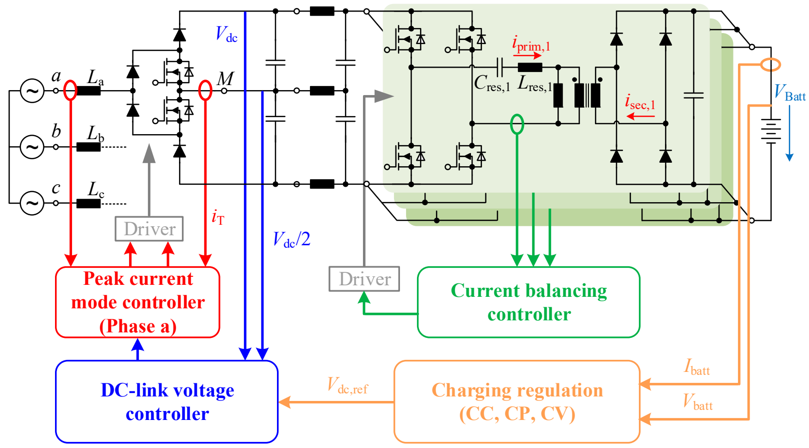

Figure 21. Two-stage system control: Peak current mode controller for PFC function (red control loop), dc-link voltage regulation and balancing (blue control loop), charging regulation (orange control loop), and power balancing of the individual LLC converter phases (green control loop).

5.2. Current Sharing in LLC Resonant Converter

By operating the LLC converter as a dc transformer, the voltage ripple is directly passed to the battery as a current ripple due to the characteristic of the resonant tank. The three-phase mains connection, however, leads to a very low ripple in the dc-link. This results in a low current ripple so that the gain of the LLC converter does not need to be regulated.

However, the synchronous parallel operation of the three individual LLC phases still poses a challenge. In the literature, the gain, respectively, and the output power of the LLC resonant converter are usually controlled by the switching frequency [61]. Due to the three separately assembled resonant circuits, the absolute values of $L_{res,x}$ and $C_{res,x}$ differ from each other, caused by deviations of the components. As a result, the series resonant frequency is different for each phase; accordingly, the resulting frequency-dependent output characteristics are shifted against each other along the frequency axis [70]. For equal distribution of the output power, an individual switching frequency must be set for each phase. However, a reduction in the resulting current ripple, due to the phase-shifted superposition of the output currents of the individual phases, cannot be achieved in this way. Instead, the different switching frequencies lead to beats in the output power, which must be filtered with additional measures. Furthermore, the design of EMI filters is hampered by the selection of a variable switching frequency, as the attenuation for the entire switching frequency range must be considered for the fundamental harmonics on the one hand and for the resulting harmonics on the other.

Instead of adjusting the switching frequency for each of the three LLC converters, all phases are operated at the same frequency in this approach. However, different resonant currents result in a higher output current ripple, unequally distributed loss, component stress, and consequently temperature, which can lead to positive feedback, further exacerbating the imbalance. To solve this problem, the modulation of the phase-shift between the two half-bridges within the driving full-bridge on the primary side is used for the control [70]. This results in a further degree of freedom, which can be used for balancing the phase currents. In addition, all primary-side MOSFETs are controlled using a common microcontroller to precisely set the phase-shift between the individual LLC converter phases to 120° without jitter or complex synchronization, thus eliminating most of the current ripple at the output.

In each of the three converter phases, the rms values of the primary and secondary resonant current i_{prim}, i_{sec}, are measured (cf. Figure 13a). The controller reduces the phase-shift for the phase with the lowest current and concurrently increases the phase-shift for the phase with the highest current. This balancing process is completed once all three LLC phases share the same primary and secondary resonant currents. Since the charging current changes only slowly over the charging time, the balancing control is implemented as a low-bandwidth PI controller, which is shown as a green control loop in Figure 21. Moreover, in the range between the end-of-discharge voltage and V_{Batt} = 740 V, the ac/dc stage operates at its minimum dc-link voltage V_{dc} = 750 V. At this operating point, the balancing control limits the primary resonant current to the preset maximum value $i_{\mathrm{prim}} = i_{\mathrm{prim,max}}$ by reducing the phase-shift of all three phases and thus, realizes the CC charging mode.

6. Experimental Verification

Based on the presented calculations and simulations, the demonstrator of an 11 kW portable off-board charger is realized, which is shown in Figure 22. The components are mainly arranged around the centrally located heatsink and are mechanically and thermally attached to it. All PCBs were designed such that large components could fill the voids between the circuit boards and passive components to improve power density. The PFC inductors are mounted directly behind the fans in a cut-out section in the heatsink, below the ac/dc stage. The hf transformers are placed in a 3D printed fixture directly in the outgoing air flow of the heatsink, which allows the windings and the core to be optimally cooled. The EMI filters are attached along the length of the charger, where the mains and battery terminals are also located. Figure 23 shows a size comparison between the assembled off-board charger and the selected CCS Combo2 vehicle connector and the CEE plug. The volume of the prototype is 4.85 dm^3 with the dimensions (L × W × H) of 225.5 mm × 244.5 mm × 88 mm. In Figure 24a, the proportions of the components to the total volume of the assembled off-board charger are shown. In Figure 24b, the proportions of the total weight are depicted. Due to the requirement for air-cooling, the heatsink contributes about 1/4 of the volume and weight of the system, which represents the largest part in both cases. The inductive components account for 22% of the total weight because of their material properties, but are of minor importance in terms of volume (only 6%) due to the high integration and the achieved high power density. The power semiconductors, the circuit boards, and the necessary control and signal electronics only account for a small proportion of the total volume (18%) and weight (12%). The EMI filters also contribute significantly to the volume and weight of the system due to the applied passive components, especially the input filter with a part of 13% each. However, as a result of the high degree of integration of all subsystems and components, the unused enclosed space in the system has been reduced to 17% (cf. Figure 24a), which corresponds to a filling factor of 83%. Accordingly, a power density of 2.3 kW/liter (37.7 W/in^3) is achieved, including heatsink, auxiliary supply, pre- and discharge circuits, and EMI filters.

The testing waveforms of the VIENNA rectifier with the 800 V battery voltage and full load are shown in Figure 25, where I_{La}, I_{Lb}, and I_{Lc} are the mains' input currents of L_a, L_b, and L_c (cf. Figure 2 or Figure 21). At full load, a power factor of 0.99 and a total harmonic distortion of the mains current of 3.8% is achieved. The harmonic current limits, defined in DIN EN 61000-2, are met up to the 40th harmonic.

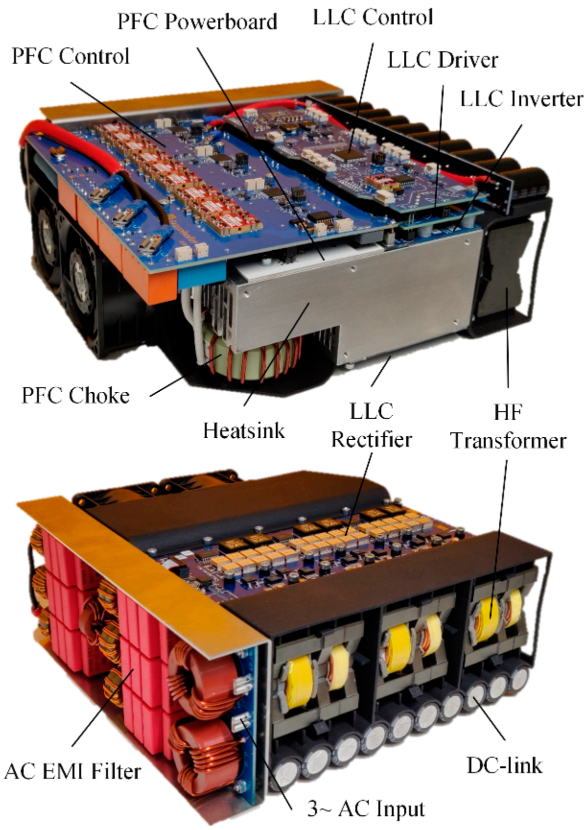

Figure 22. Prototype of the proposed portable off-board charger. The dc EMI filter is removed in the upper picture to provide a view of the PFC inductors and the hf transformers placed inside the heatsink.

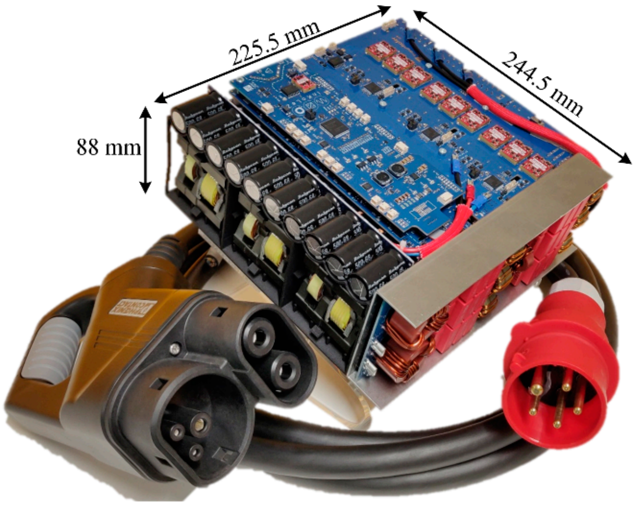

Figure 23. Top view of the 11 kW charging converter with dimensioned edge lengths. The selected CCS Combo2 vehicle connector and the CEE plug are shown for size comparison of the assembled off-board charger.

The measured key waveforms of the LLC resonant converter are shown in Figure 26 at full load and with an 800 V battery voltage. In Figure 26, v_{prim} and i_{prim} are the input voltage and input current of the resonant tank, respectively, v_{sec} and i_{sec} are the output voltage and output current of the transformer on the secondary. The primary inverter switches turn-on at negative i_{prim} and thus achieves ZVS. By selecting the operating point slightly below the series resonance, the secondary-side resonant current i_{sec} becomes zero before the end of the switching period and the rectifier diodes turn off under the ZCS conditions.

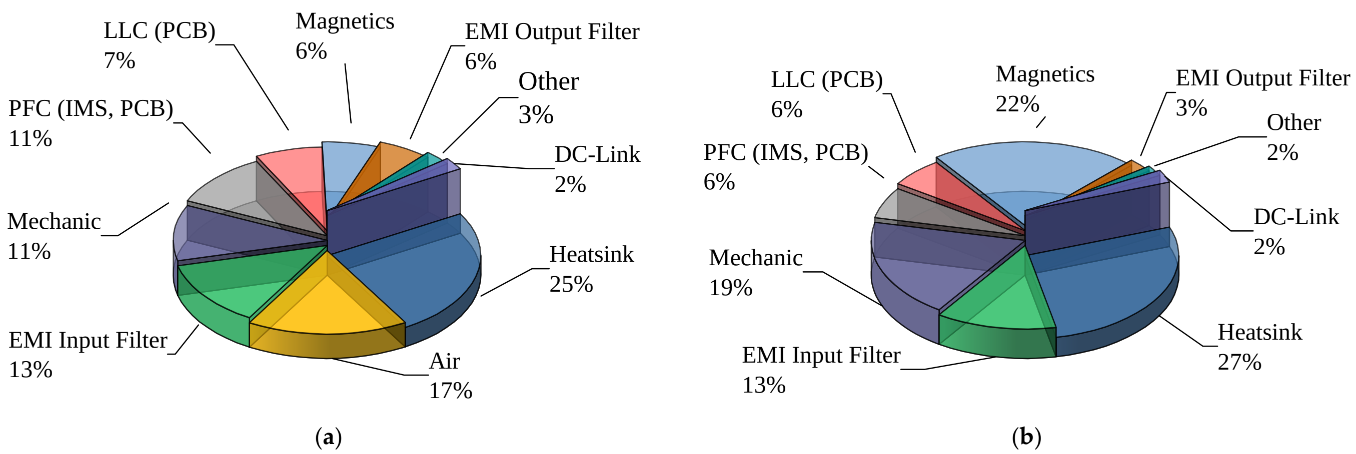

Figure 24. Breakdown of the system components according to their contribution to (**a**) the volume of the charger of 4.85 L and (**b**) the mass of the charger of 5.78 kg.

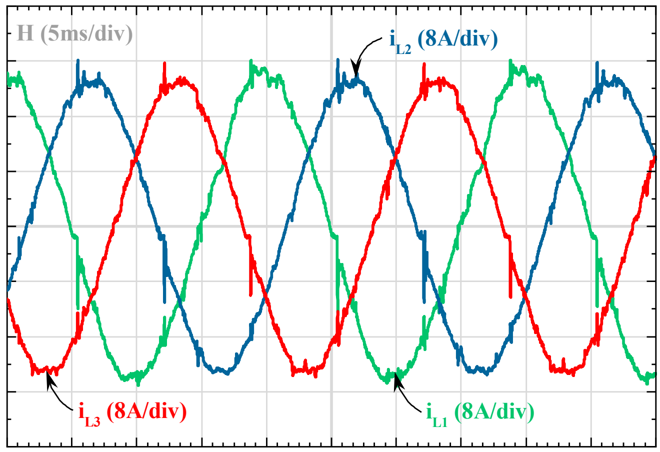

Figure 25. Experimental waveforms of the VIENNA rectifier with 800 V battery voltage and full load (P_{ac} = 11 kW).

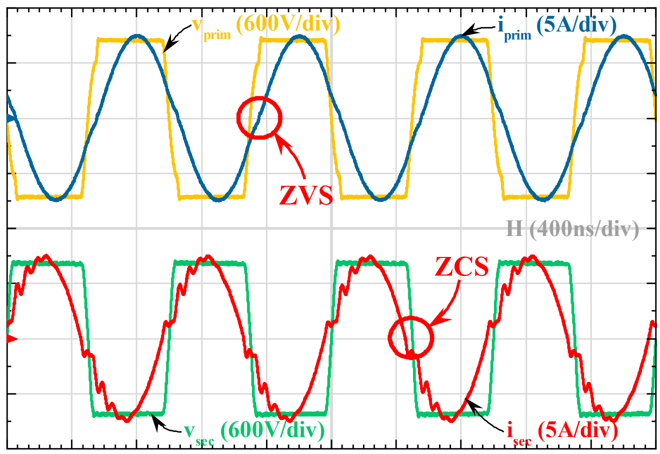

Figure 26. Experimental waveforms of single-phase operation of the dc/dc stage with 800 V battery voltage and full load (P_{LLC} = 3.5 kW).

The operating waveforms of all three LLC phases are shown in Figure 27. At the tested operating point at full load and with an 800 V battery voltage, phase 2 of the LLC converter is exposed to the highest load ($\hat{\imath}_{\mathrm{prim},2}$ = 8.4 A), phase 3 to a medium load ($\hat{\imath}_{\mathrm{prim},3}$ = 7.7 A) and phase 1 to the lowest load ($\hat{\imath}_{\mathrm{prim},1}$ = 7 A) (cf. Figure 27a). With active balancing control, the amplitudes of $i_{\mathrm{prim,x}}$ for all three phases are equalized to the same peak ($\hat{\imath}_{\mathrm{prim,x}}$ = 7.5 A) and rms values (see Figure 27b). Therefore, the control reduces the phase-shift of phase 2 and increases the phase-shift for phase 1 until the balancing process is completed. The precise superposition of the output currents of the three LLC converter phases reduces the peak-to-peak ripple of the charging current into the battery to less than 0.3 A.

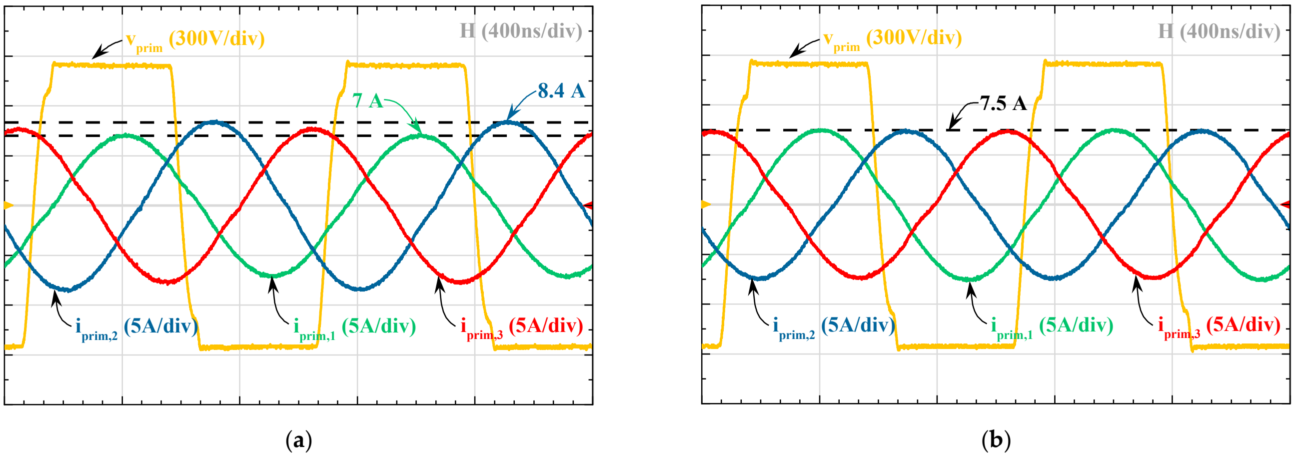

Figure 27. Experimental waveforms of three-phase operation of the dc/dc stage with 800 V battery voltage and full load (P_{ac} = 11 kW) with (**a**) symmetry control inactive and (**b**) symmetry control active.

The measured efficiency of the portable off-board charger is shown in Figure 28. For 400 V_{AC} mains voltage, a total efficiency of 95.8% is achieved over the entire battery voltage range, the maximum efficiency reaches 96% at 800 V battery voltage and a charging power of 9 kW. Compared with the state-of-the-art on-board chargers build by industry and academia in Figure 1, the portable off-board charger is among the best 20% of the evaluated systems. The VIENNA rectifier achieves an efficiency of above 97% from 1 kW output power and reaches efficiencies of 98% at nominal power over a wide output voltage range. According to Figure 28, the three LLC converters operated in parallel achieve a high efficiency of 97.7% over a wide range of the battery voltages.

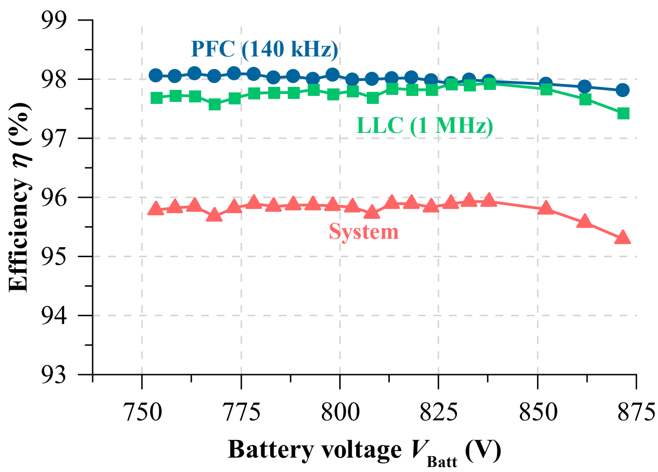

Figure 28. Measured efficiency of the VIENNA PFC, the three-phase LLC resonant converter, and the entire system under full load.

To evaluate the performance of the optimized hf transformer and the resonant inductance, a single phase of the LLC converter is analyzed separately. Figure 29 shows the measured efficiency plotted versus the output power at an output voltage of 800 V when driving the primary-side full-bridge with a 50% duty cycle. Thereby, the output power is adjusted by varying the input voltage. An efficiency of over 96% is already achieved at 1 kW output power, which increases to 98.12% at nominal power. Compared to the efficiency of the total system in Figure 28, this value is higher as the three individual LLC converters are controlled with different duty cycles using the balancing control. Therefore, the efficiency of the individual phases decreases slightly with reduced duty cycles, which leads to a lower overall value.

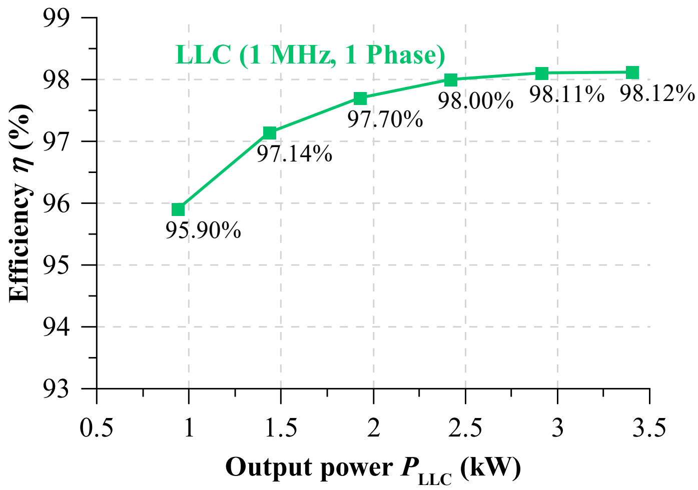

Figure 29. Measured efficiency of a single phase of the LLC resonant converter plotted versus the output power at 800 V battery voltage and driving of the primary inverter switches with a fixed 50% duty cycle.

The thermal behavior is also tested with the prototype, as shown in Figure 30. The measured temperatures are determined after reaching a steady state at 24 °C room temperature, and the fans are operated at 60% of their rated power. At a charging power of 11 kW and an efficiency of 95.8% at a battery voltage of 800 V, the total thermal losses add up to 482 W. It can be observed, that the hottest spot with 87 °C is located inside the winding in the area of the center leg of the optimized hf transformer. A comprehensive comparison between the proposed portable off-board charger and other state-of-the-art galvanically isolated on-board chargers is shown in Table 9 (cf. Figure 1).

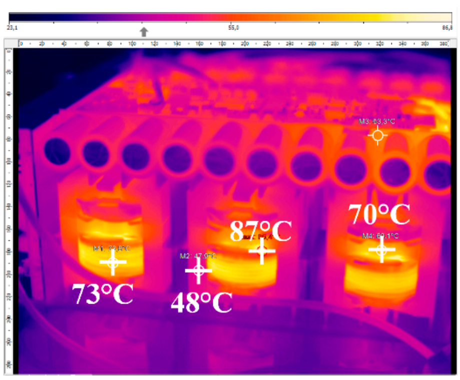

(**a**)

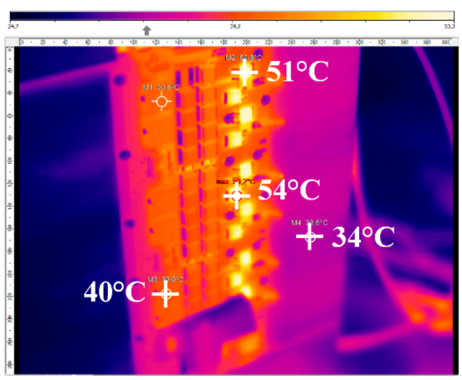

(**b**)

Figure 30. Thermal image of the prototype operating at full load. (**a**) View on hf transformers; (**b**) view on secondary-side rectifier.

Table 9. Comparison between the proposed portable off-board charger and other state-of-the-art galvanically isolated on-board chargers.

References	Efficiency (%)	Cooling	Characteristics
[5]	96	air-cooled	• Bidir. 300 kHz LLC resonant converter • WBG SiC devices, Totem Pole PFC, 6.6 kW
[6]	96.2	water-cooled	• Bidir. 500 kHz CLLC resonant converter • WBG SiC devices, Totem Pole PFC, 6.6 kW • Variable dc-link voltage control
[7]	94.7	water-cooled	• Bidir. 80 kHz CLLC resonant converter • WBG GaN devices, Totem Pole PFC, 6 kW • Variable transformer turns ratio, modular
[8]	94.7	air-cooled	• Unidir. 200 kHz phase-shifted full-bridge • WBG SiC devices, bridgeless boost PFC • 6 kW, no EMI filter considered
[9]	96	air-cooled	• Bidir. 200 kHz CLLC resonant converter • WBG SiC devices, Totem Pole PFC, 6.6 kW
[10]	94	water-cooled	• Unidir. 315 kHz CLLC resonant converter • Silicon devices, Boost PFC, 3.7 kW
[12]	97	air-cooled	• Unidir. 500 kHz DAB converter • WBG GaN devices, active rectifier, 7.2 kW • No EMI filter considered, no DC-link
Our proposal	95.8	air-cooled	• Unidir. 1000 kHz LLC resonant converter • WBG SiC devices, VIENNA PFC, 11 kW

7. Conclusions

In this paper, a portable 11 kW off-board charger for electric vehicles with 800 V battery technology is proposed. For the active PFC rectifier, different candidates are evaluated and compared, and the VIENNA topology is selected together with a variable dc-link voltage concept. Using analytical calculations, the loss and volume of the PFC inductance are optimized over a wide range of input parameters. Considering the calculated power semiconductor losses of the active VIENNA rectifier, the optimum PFC coil is selected and manufactured for the chosen switching frequency. For the galvanically isolated dc/dc stage, a three-phase LLC resonant converter operating at 1 MHz is selected. A parametrizable loss model of the hf transformer and the resonance inductor is developed to minimize volume, weight, and losses. Using these models with an automated algorithm, the inductive components are optimized in terms of winding specification, choice of the magnetic material, and design of the core geometry. For the selected switching frequency of 1 MHz, a transformer with external but attached resonant inductance, which shares part of the transformer's magnetic path, is built, and the results are verified by finite element analysis and measurements. Finally, a mechatronically integrated portable air-cooled off-board charger prototype with 11 kW, a three-phase 400 V_{AC} input, and a 620–850 V_{DC} output using SiC devices was built and tested. The prototype demonstrates a peak efficiency of 96% with 95.8% efficiency over the battery voltage range, while one phase of the optimized LLC resonant converter achieves a peak efficiency of 98.12% at 1 MHz and full load. With the compact dimensions of the inductive components and a high level of mechatronic integration, a power density of the entire system of 2.3 kW/liter (37.7 W/in^3) is reached, including heatsink, EMI filter, auxiliary power supply, and pre- and discharge circuits.

Author Contributions: Conceptualization, S.D.; methodology, S.D., S.E., M.S. and N.W.; software, P.M. and F.A.; validation, F.A., P.M. and C.S.; formal analysis, S.D., S.E., M.S. and N.W.; resources, S.D., S.E., M.S. and P.M.; writing—original draft preparation, S.D., S.E. and N.W.; writing—review and editing, A.S.; project administration, S.D.; funding acquisition, C.J. All authors have read and agreed to the published version of the manuscript.

Funding: This research was funded by the Federal Ministry of Education and Research of Germany in the framework of InKoLeZ, grant number 16EMO0238. This project has received funding from the ECSEL Joint Undertaking (JU) under grant agreement No 101007229. The JU receives support from the European Union's Horizon 2020 research and innovation programme and Germany, France, Belgium, Austria, Sweden, Spain, and Italy.

Acknowledgments: The authors would like to thank M. Schmidhuber, C. Drexler, and H. Jungwirth from SUMIDA Components & Modules GmbH, Obernzell, Germany, for the production and assembly of the required inductive components.

Conflicts of Interest: The authors declare no conflict of interest. The funders had no role in the design of the study; in the collection, analyses, or interpretation of data; in the writing of the manuscript, or in the decision to publish the results.

References

1. Ahmad, A.; Alam, M.S.; Chabaan, R. A Comprehensive Review of Wireless Charging Technologies for Electric Vehicles. *IEEE Trans. Transp. Electrif.* **2018**, *4*, 38–63. [CrossRef]
2. Mahone, A.; Subin, Z.; Orans, R.; Miller, M.; Regan, L.; Calviou, M.; Saenz, M.; Bacalao, N. On the Path to Decarbonization: Electrification and Renewables in California and the Northeast United States. *IEEE Power Energy Mag.* **2018**, *16*, 58–68. [CrossRef]
3. Fulli, G.; Masera, M.; Spisto, A.; Vitiello, S. A Change is Coming: How Regulation and Innovation Are Reshaping the European Union's Electricity Markets. *IEEE Power Energy Mag.* **2019**, *17*, 53–66. [CrossRef]
4. Khaligh, A.; D'Antonio, M. Global Trends in High-Power On-Board Chargers for Electric Vehicles. *IEEE Trans. Veh. Technol.* **2019**, *68*, 3306–3324. [CrossRef]
5. Li, H.; Zhang, Z.; Wang, S.; Tang, J.; Ren, X.; Chen, Q. A 300-kHz 6.6-kW SiC Bidirectional LLC Onboard Charger. *IEEE Trans. Ind. Electron.* **2020**, *67*, 1435–1445. [CrossRef]
6. Li, B.; Li, Q.; Lee, F.C.; Liu, Z.; Yang, Y. A High-Efficiency High-Density Wide-Bandgap Device-Based Bidirectional On-Board Charger. *IEEE J. Emerg. Sel. Top. Power Electron.* **2018**, *6*, 1627–1636. [CrossRef]
7. Endres, S.; Sessler, C.; Zeltner, S.; Eckardt, B.; Morita, T. 6 kW Bidirectional, Insulated On-board Charger with Normally-Off GaN Gate Injection Transistors. In *PCIM Europe 2017; International Exhibition and Conference for Power Electronics, Intelligent Motion, Renewable Energy and Energy Management*; VDE: Nuremberg, Germany, 2017; pp. 1–6.
8. Whitaker, B.; Barkley, A.; Cole, Z.; Passmore, B.; Martin, D.; McNutt, T.R.; Lostetter, A.B.; Lee, J.S.; Shiozaki, K. A High-Density, High-Efficiency, Isolated On-Board Vehicle Battery Charger Utilizing Silicon Carbide Power Devices. *IEEE Trans. Power Electron.* **2014**, *29*, 2606–2617. [CrossRef]
9. Wei, C.; Shao, J.; Agrawal, B.; Zhu, D.; Xie, H. New Surface Mount SiC MOSFETs Enable High Efficiency High Power Density Bi-directional On-Board Charger with Flexible DC-link Voltage. In Proceedings of the 2019 IEEE Applied Power Electronics Conference and Exposition (APEC), Anaheim, CA, USA, 17–21 March 2019; pp. 1904–1909.
10. Schmenger, J.; Endres, S.; Zeltner, S.; März, M. A 22 kW on-board charger for automotive applications based on a modular design. In Proceedings of the 2014 IEEE Conference on Energy Conversion (CENCON), Johor Bahru, Malaysia, 13–14 October 2014; pp. 1–6.
11. Gautam, D.S.; Musavi, F.; Edington, M.; Eberle, W.; Dunford, W.G. An Automotive Onboard 3.3-kW Battery Charger for PHEV Application. *IEEE Trans. Veh. Technol.* **2012**, *61*, 3466–3474. [CrossRef]
12. Lu, J.; Liu, G.; Bai, H.; Brown, A.; Johnson, P.M.; McAmmond, M.; Taylor, A.R. Applying Variable-Switching-Frequency Variable-Phase-Shift Control and E-Mode GaN HEMTs to an Indirect Matrix Converter-Based EV Battery Charger. *IEEE Trans. Transp. Electrif.* **2017**, *3*, 554–564. [CrossRef]
13. Tang, Y.; Lu, J.; Wu, B.; Zou, S.; Ding, W.; Khaligh, A. An Integrated Dual-Output Isolated Converter for Plug-in Electric Vehicles. *IEEE Trans. Veh. Technol.* **2018**, *67*, 966–976. [CrossRef]
14. BRUSA Elektronik, AG. NLG667—On Board Fast Charger. Available online: https://www.brusa.biz/produkte/ladetechnik/ladegeraete-750-v/nlg667.html (accessed on 18 March 2020).
15. AVID Technology Limited. Onboard Battery Charger: 22kW SAE J1772 On Board Charger Solution for Electric and Hybrid Vehicles, Available with Output Voltage up to 850V. Available online: https://avidtp.com/product/onboard-charger/ (accessed on 29 April 2022).
16. FinePower GmbH. Automotive Isolated Onboard Charger for EV/HEV. Available online: https://www.finepower.com/wp-content/uploads/2017/11/Datasheet_Automotive_isolated_onboard-charger_web.pdf (accessed on 29 April 2022).

17. Innolectric AG. On-Board Charger: Efficient Power Electronics for AC and DC Charging. On-Board Charger OBC82. Available online: https://innolectric.ag/wp-content/uploads/2020/03/innolectric_On-Board_Charger_E2_2002-1.pdf (accessed on 29 April 2022).
18. Stercom GmbH. OnBoard Charger OBC_22kW. Available online: https://stercom.de/en/service/downloads.html (accessed on 24 March 2020).
19. Current Ways Inc. CWBC Series 6.6kW Bi-Directional EV On Board Charger. Available online: https://currentways.com/wp-content/uploads/2013/10/CWBC-Series-6.6kW-Bi-directional-OBC-Liquid-Cooled-050918.pdf (accessed on 29 April 2022).
20. Current Ways Inc. BC-Series 3kW 112-450 Volt IP67 Rated Air-Cooled EV Battery Charger. Available online: https://currentways.com/wp-content/uploads/2013/10/ds-air-225.pdf (accessed on 29 April 2022).
21. Ovar Clean Energy Technology Co., Ltd. EV On-Board Charger: Model CAD332DF-400A 3.3 kW. Available online: https://www.ovartech.com/wp-content/uploads/2017/12/3.3KW-OBC-CAD332DF-400A.pdf (accessed on 29 April 2022).
22. Friedli, T.; Hartmann, M.; Kolar, J.W. The Essence of Three-Phase PFC Rectifier Systems—Part II. *IEEE Trans. Power Electron.* **2014**, *29*, 543–560. [CrossRef]
23. Prasad, R.; Namuduri, C.; Kollmeyer, P. Onboard unidirectional automotive G2V battery charger using sine charging and its effect on li-ion batteries. In Proceedings of the 2015 IEEE Energy Conversion Congress and Exposition (ECCE), Montreal, QC, Canada, 20–24 September 2015; pp. 6299–6305.
24. Jung, C. Power Up with 800-V Systems: The benefits of upgrading voltage power for battery-electric passenger vehicles. *IEEE Electrif. Mag.* **2017**, *5*, 53–58. [CrossRef]
25. Porsche Newsroom. The Charging Process: Quick, Comfortable, Intelligent and Universal. Available online: https://newsroom.porsche.com/en/products/taycan/charging-18558.html (accessed on 28 April 2022).
26. Bowermaster, D.; Alexander, M.; Duvall, M. The Need for Charging: Evaluating utility infrastructures for electric vehicles while providing customer support. *IEEE Electrif. Mag.* **2017**, *5*, 59–67. [CrossRef]
27. Liu, Z.; Lee, F.C.; Li, Q.; Yang, Y. Design of GaN-Based MHz Totem-Pole PFC Rectifier. *IEEE J. Emerg. Sel. Top. Power Electron.* **2016**, *4*, 799–807. [CrossRef]
28. Endruschat, A.; Novak, C.; Gerstner, H.; Heckel, T.; Joffe, C.; März, M. A Universal SPICE Field-Effect Transistor Model Applied on SiC and GaN Transistors. *IEEE Trans. Power Electron.* **2019**, *34*, 9131–9145. [CrossRef]
29. Ehrlich, S.; Rossmanith, H.; Sauer, M.; Joffe, C.; März, M. Fast Numerical Power Loss Calculation for High-Frequency Litz Wires. *IEEE Trans. Power Electron.* **2021**, *36*, 2018–2032. [CrossRef]
30. *IEC 61851-23:2014*; Electric Vehicle Conductive Charging System—Part 23: DC Electric Vehicle Charging Station. IEC: Geneva, Switzerland, 2014.
31. *IEC 62196-1:2014*; Plugs, Socket-Outlets, Vehicle Connectors and Vehicle Inlets—Conductive Charging of Electric Vehicles—Part 1, 2, 3. IEC: Geneva, Switzerland, 2014.
32. Phoenix Contact. Charging Technology for Electromobility—Product Overview 2019/2020. Available online: https://www.phoenixcontact.com/assets/2018/interactive_ed/101_142148/epaper/CAT_7_2019_EN_LoRes.pdf (accessed on 28 April 2022).
33. Kolar, J.W.; Friedli, T. The Essence of Three-Phase PFC Rectifier Systems—Part I. *IEEE Trans. Power Electron.* **2013**, *28*, 176–198. [CrossRef]
34. Wang, X.; Jiang, C.; Lei, B.; Teng, H.; Bai, H.K.; Kirtley, J.L. Power-Loss Analysis and Efficiency Maximization of a Sili-con-Carbide MOSFET-Based Three-Phase 10-kW Bidirectional EV Charger Using Variable-DC-Bus Control. *IEEE J. Emerg. Sel. Top. Power Electron.* **2016**, *4*, 880–892. [CrossRef]
35. Kolar, J.W.; Zach, F.C. A Novel Three-Phase Three-Switch Three-Level PWM Rectifier. In Proceedings of the 28th Power conversion Conference, Nürnberg, Germany, 28–30 June 1994; pp. 125–138.
36. Guan, Q.; Li, C.; Zhang, Y.; Wang, S.; Xu, D.D.; Li, W.; Ma, H. An Extremely High Efficient Three-Level Active Neu-tral-Point-Clamped Converter Comprising SiC and Si Hybrid Power Stages. *IEEE Trans. Power Electron.* **2018**, *33*, 8341–8352. [CrossRef]
37. Rodriguez, J.; Lai, J.-S.; Peng, F.Z. Multilevel inverters: A survey of topologies, controls, and applications. *IEEE Trans. Ind. Electron.* **2002**, *49*, 724–738. [CrossRef]
38. Stupar, A.; Friedli, T.; Minibock, J.; Kolar, J.W. Towards a 99% Efficient Three-Phase Buck-Type PFC Rectifier for 400-V DC Distribution Systems. *IEEE Trans. Power Electron.* **2012**, *27*, 1732–1744. [CrossRef]
39. Schrittwieser, L.; Leibl, M.; Haider, M.; Thony, F.; Kolar, J.W.; Soeiro, T.B. 99.3% Efficient Three-Phase Buck-Type All-SiC SWISS Rectifier for DC Distribution Systems. *IEEE Trans. Power Electron.* **2019**, *34*, 126–140. [CrossRef]
40. Heckel, T.; Rettner, C.; März, M. Fundamental efficiency limits in power electronic systems. In Proceedings of the 2015 IEEE International Tele-communications Energy Conference (INTELEC), Osaka, Japan, 18–22 October 2015; pp. 1–6.
41. Albach, M. *Induktivitäten in der Leistungselektronik: Spulen, Trafos und ihre Parasitären Eigenschaften*; Springer: Wiesbaden, Germany, 2017; ISBN 978-3-658-15080-8.
42. *IEC 60205:2016*; Calculation of the Effective Parameters of Magnetic Piece Parts. IEC: Geneva, Switzerland, 2016.
43. Magnetics A Division of Spang & Company. Effects of Temperature on Core Loss of Alloy Powder Cores. Available online: https://www.mag-inc.com/Media/Magnetics/File-Library/Product%20Literature/Powder%20Core%20Literature/Effects-of-Temperature-on-Core-Loss-of-Alloy-Powder-Cores.pdf?ext=.pdf (accessed on 30 May 2022).

44. Albach, M.; Durbaum, T.; Brockmeyer, A. Calculating Core Losses in Transformers for Arbitrary Magnetizing Currents a Comparison of Different Approaches. In Proceedings of the PESC Record. 27th Annual IEEE Power Electronics Specialists Conference, Baveno, Italy, 23–27 June 1996; pp. 1463–1468.
45. Muhlethaler, J.; Biela, J.; Kolar, J.W.; Ecklebe, A. Core Losses Under the DC Bias Condition Based on Steinmetz Parameters. *IEEE Trans. Power Electron.* **2012**, *27*, 953–963. [CrossRef]
46. Albach, M. Two-dimensional calculation of winding losses in transformers. In Proceedings of the 2000 IEEE 31st Annual Power Electronics Spe-cialists Conference. Conference Proceedings (Cat. No.00CH37018), Galway, Ireland, 18–23 June 2000; pp. 1639–1644.
47. Wang, H.; Dusmez, S.; Khaligh, A. Maximum Efficiency Point Tracking Technique for LLC-Based PEV Chargers Through Variable DC Link Control. *IEEE Trans. Ind. Electron.* **2014**, *61*, 6041–6049. [CrossRef]
48. Deng, J.; Mi, C.C.; Ma, R.; Li, S. Design of LLC Resonant Converters Based on Operation-Mode Analysis for Level Two PHEV Battery Chargers. *IEEE/ASME Trans. Mechatron.* **2015**, *20*, 1595–1606. [CrossRef]
49. Xu, H.; Yin, Z.; Zhao, Y.; Huang, Y. Accurate Design of High-Efficiency LLC Resonant Converter With Wide Output Voltage. *IEEE Access* **2017**, *5*, 26653–26665. [CrossRef]
50. Suryawanshi, H.M.; Talapur, G.G.; Ballal, M.S. Optimized Resonant Converter by Implementing Shunt Branch Element as Magnetizing Inductance of Transformer in Electric Vehicle Chargers. *IEEE Trans. Ind. Appl.* **2019**, *55*, 7471–7480. [CrossRef]
51. He, P.; Mallik, A.; Sankar, A.; Khaligh, A. Design of a 1-MHz High-Efficiency High-Power-Density Bidirectional GaN-Based CLLC Converter for Electric Vehicles. *IEEE Trans. Veh. Technol.* **2019**, *68*, 213–223. [CrossRef]
52. Zhang, Z.; Liu, C.; Wang, M.; Si, Y.; Liu, Y.; Lei, Q. High-Efficiency High-Power-Density CLLC Resonant Converter with Low-Stray-Capacitance and Well-Heat-Dissipated Planar Transformer for EV On-Board Charger. *IEEE Trans. Power Electron.* **2020**, *35*, 10831–10851. [CrossRef]
53. Li, B.; Li, Q.; Lee, F.C. High-Frequency PCB Winding Transformer With Integrated Inductors for a Bi-Directional Resonant Converter. *IEEE Trans. Power Electron.* **2019**, *34*, 6123–6135. [CrossRef]
54. Ren, X.; Xu, Z.; Zhang, Z.; Li, H.; He, M.; Tang, J.; Chen, Q. A 1-kV Input SiC LLC Converter With Split Resonant Tanks and Matrix Transformers. *IEEE Trans. Power Electron.* **2019**, *34*, 10446–10457. [CrossRef]
55. Zou, S.; Lu, J.; Mallik, A.; Khaligh, A. Modeling and Optimization of an Integrated Transformer for Electric Vehicle On-Board Charger Applications. *IEEE Trans. Transp. Electrif.* **2018**, *4*, 355–363. [CrossRef]
56. Zhang, J.; Ouyang, Z.; Duffy, M.C.; Andersen, M.A.E.; Hurley, W.G. Leakage Inductance Calculation for Planar Transformers With a Magnetic Shunt. *IEEE Trans. Ind. Appl.* **2014**, *50*, 4107–4112. [CrossRef]
57. Biela, J.; Kolar, J.W. Electromagnetic integration of high power resonant circuits comprising high leakage inductance transformers. In Proceedings of the 2004 IEEE 35th Annual Power Electronics Specialists Conference, Aachen, Germany, 20–25 June 2004; pp. 4537–4545.
58. Saket, M.A.; Shafiei, N.; Ordonez, M. LLC Converters With Planar Transformers: Issues and Mitigation. *IEEE Trans. Power Electron.* **2017**, *32*, 4524–4542. [CrossRef]
59. Lazar, J.F.; Martinelli, R. Steady-state analysis of the LLC series resonant converter. In Proceedings of the APEC 2001. Sixteenth Annual IEEE Applied Power Electronics Conference and Exposition (Cat. No.01CH37181), Anaheim, CA, USA, 4–8 March 2001; pp. 728–735.
60. Ditze, S.; Heckel, T.; März, M. Influence of the junction capacitance of the secondary rectifier diodes on output characteristics in multi-resonant converters. In Proceedings of the 2016 IEEE Applied Power Electronics Conference and Exposition (APEC), Long Beach, CA, USA, 20–24 March 2016; pp. 864–871.
61. Lu, B.; Liu, W.; Liang, Y.; Lee, F.C.; van Wyk, J.D. Optimal design methodology for LLC resonant converter. In Proceedings of the Twenty-First Annual IEEE Applied Power Electronics Conference and Exposition, 2006. APEC '06, Dallas, TX, USA, 19–23 March 2006. [CrossRef]
62. Kundu, U.; Yenduri, K.; Sensarma, P. Accurate ZVS Analysis for Magnetic Design and Efficiency Improvement of Full-Bridge LLC Resonant Converter. *IEEE Trans. Power Electron.* **2017**, *32*, 1703–1706. [CrossRef]
63. Kazimierczuk, M.K.; Czarkowski, D. *Resonant Power Converters, 2. Auflage*; Wiley-IEEE Press: New York, NY, USA, 2012, ISBN 0470905387.
64. McLyman, C.W.T. *Transformer and Inductor Design Handbook*, 3rd ed.; rev. and expanded; Dekker: New York, NY, USA, 2004, ISBN 0824753933.
65. Li, J.; Abdallah, T.; Sullivan, C.R. Improved calculation of core loss with nonsinusoidal waveforms. In Proceedings of the Conference Record of the 2001 IEEE Industry Applications Conference. 36th IAS Annual Meeting (Cat. No.01CH37248), Chicago, IL, USA, 30 September–4 October 2001; Volume 4, pp. 2203–2210. [CrossRef]
66. Sullivan, C.R. Optimal choice for number of strands in a litz-wire transformer winding. *IEEE Trans. Power Electron.* **1999**, *14*, 283–291. [CrossRef]
67. Kolar, J.W.; Neumayr, D.; Bortis, D. The Google Little Box Challenge—Ultra-Compact GaN- or SiC-Based Single-Phase DC/AC Power Conversion. In Proceedings of the 19th European Conference on Power Electronics and Applications (EPE'17—ECCE Europe), Warsaw, Poland, 11–14 September 2017. [CrossRef]

68. Stolzke, T.; Ehrlich, S.; Joffe, C.; März, M. Comprehensive accuracy examination of electrical power loss measurements of inductive components for frequencies up to 1 MHz. *J. Magn. Magn. Mater.* **2020**, *497*, 166022. [CrossRef]
69. Erickson, R.W.; Maksimović, D. *Fundamentals of Power Electronics*, 2nd ed.; 6 printing; Kluwer Academic Publishers: Norwell, MA, USA, 2004, ISBN 0792372700.
70. Arshadi, S.A.; Ordonez, M.; Eberle, W.; Saket, M.A.; Craciun, M.; Botting, C. Unbalanced Three-Phase LLC Resonant Converters: Analysis and Trigonometric Current Balancing. *IEEE Trans. Power Electron.* **2019**, *34*, 2025–2038. [CrossRef]